DESIGN AND ANALYSIS OF UWB ANTENNAS FOR MICROWAVE IMAGING BASED MEDICAL APPLICATIONS

ANTORA HOSSAIN (SN. 0420160001)

A Thesis Submitted in Partial Fulfillment of the Requirements for the Degree of Master of Science in Electrical, Electronic and Communication Engineering

DEPARTMENT OF ELECTRICAL, ELECTRONIC AND COMMUNICATION ENGINEERING
MILITARY INSTITUTE OF SCIENCE AND TECHNOLOGY
DHAKA, BANGLADESH

MARCH 2023

DESIGN AND ANALYSIS OF UWB ANTENNAS FOR MICROWAVE IMAGING BASED MEDICAL APPLICATIONS

M.Sc. Engineering Thesis

By

ANTORA HOSSAIN (SN. 0420160001)

Approved as to style and content by the Board of Examination on 07 March 2023:

_____ Major Md Aminul Islam, PhD Instructor Class B of EECE Department MIST, Dhaka	Chairman (Supervisor) Board of Examination
_____ Dr. Pran Kanai Saha Professor of EEE Department BUET, Dhaka	Member (External) Board of Examination
_____ Dr. Md. Hossam-E-Haider Professor of EECE Department MIST, Dhaka	Member (Internal) Board of Examination
_____ Brig Gen Md Mahfuzul Karim Majumder Dean of Faculty of ECE MIST, Dhaka	Member (Ex-officio) Board of Examination

Department of EECE, MIST, Dhaka

DESIGN AND ANALYSIS OF UWB ANTENNAS FOR MICROWAVE IMAGING BASED MEDICAL APPLICATIONS

DECLARATION

I hereby declare that the study reported in this thesis entitled as above is my own original work and has not been submitted before anywhere for any degree or other purposes. Further I certify that the intellectual content of this thesis is the product of my own work and that all the assistance received in preparing this thesis and sources have been acknowledged or cited in the reference Section.

_____

Antora Hossain

Department of EECE, MIST, Dhaka

ABSTRACT

Design and Analysis of UWB Antennas for Microwave Imaging Based Medical Applications

Microwave imaging is renowned as one of the most promising technologies in the medical application of abnormality or lesion diagnosis. The underlying concept of active microwave imaging is to diagnose a lesion by evaluating the large dielectric difference between normal tissue and abnormal tissue employing antennas as the key element. A salient feature of microwave imaging antenna is attributed to its ultra-wide impedance bandwidth as found in the previous research works. In this research work, an ultra-wideband (UWB) bow-tie antenna and a monopole antenna are designed and analyzed for simultaneous detection and localization of brain tumor and brain stroke respectively using a microwave imaging technique. The bandwidth enhancement of the proposed bow-tie antenna is accomplished by dint of a self-complementary structure while the bandwidth of the proposed monopole antenna is enhanced with defected ground structure (DGS) and trident-shaped feeding strip. Furthermore, a six-layered human head phantom composed of skin, fat, bone, dura, cerebrospinal fluid (CSF), and brain is modeled in which a malignant tumor, hemorrhagic stroke, and ischemic stroke are inserted individually upholding the safety regulation of specific absorption rate (SAR). In addition, the monostatic radar-based delay-and-sum (DAS) beam-forming or confocal microwave imaging algorithm is developed for visualizing the location of the lesion explicitly via image reconstruction. It is exposed from the simulation results that the proposed bow-tie antenna achieves superior performance to the conventional counterparts, specifically, in respect of bandwidth and radiation efficiency whereas the proposed monopole antenna attains superiority regarding bandwidth and size in particular. Brain tumor detection is assured with a drastic improvement of current density and SAR of the proposed bow-tie antenna compared to the normal healthy tissue. However, the hemorrhagic stroke is detected with an excess of current density and SAR of the proposed monopole antenna in comparison to the healthy brain while the situation reverses in the case of the ischemic stroke. Eventually, the relevant microwave images are reconstructed reliably in two-dimension with a high spatial resolution. Hence, the proposed research work might save human lives by the alleviation of mortality rate due to brain abnormalities through an early and quick diagnosis.

সারসংক্ষেপ

Design and Analysis of UWB Antennas for Microwave Imaging Based Medical Applications

অস্বাভাবিকতা বা ক্ষত নির্ণয়ের চিকিৎসা প্রয়োগে মাইক্রোওয়েভ ইমেজিং অন্যতম প্রতিশ্রুতিশীল প্রযুক্তি হিসেবে বিখ্যাত। সক্রিয় মাইক্রোওয়েভ ইমেজিংয়ের অন্তর্নিহিত ধারণাটি হল অ্যান্টেনাকে অপরিহার্য অংশ হিসেবে ব্যবহার করে স্বাভাবিক টিস্যু এবং অস্বাভাবিক টিস্যুর মধ্যে বৃহৎ পরাবৈদ্যুতিক পার্থক্য মূল্যায়নের মারফত একটি ক্ষত নির্ণয় করা। মাইক্রোওয়েভ ইমেজিং অ্যান্টেনার একটি লক্ষণীয় বৈশিষ্ট্য এর আল্ট্রা-ওয়াইড ইম্পিডেন্স ব্যান্ডউইথের উপর আরোপিত যেমনটি পূর্ববর্তী গবেষণা কাজসমূহে পাওয়া যায়। এই গবেষণার কাজে, একটি আল্ট্রা-ওয়াইডব্যান্ড (UWB) বো-টাই অ্যান্টেনা এবং একটি মনোপোল অ্যান্টেনা একটি মাইক্রোওয়েভ ইমেজিং কৌশল ব্যবহার করে যথাক্রমে মস্তিষ্কের টিউমার এবং মস্তিষ্কের স্ট্রোকের একযোগে সনাক্তকরণ এবং অবস্থান নির্ধারণের জন্য উদ্ভাবন এবং বিশ্লেষণ করা হয়েছে। প্রস্তাবিত বো-টাই অ্যান্টেনাটির ব্যান্ডউইথ বর্ধন একটি স্ব-পরিপূরক কাঠামোর সাহায্যে সম্পন্ন করা হয় যখন প্রস্তাবিত মনোপোল অ্যান্টেনাটির ব্যান্ডউইথ ত্রুটিযুক্ত ভূতল কাঠামো (DGS) এবং ত্রিশূল-আকৃতির ফিডিং স্ট্রিপ দ্বারা বর্ধিত করা হয়। অধিকন্তু, ত্বক, চর্বি, হাড়, ডুরা, সেরিব্রোস্পাইনাল ফ্লুইড (CSF), এবং মস্তিষ্কের সমন্বয়ে গঠিত একটি ছয়-স্তরবিশিষ্ট মানুষের মাথার ফ্যান্টম স্থাপিত হয় যার মধ্যে নির্দিষ্ট শোষণ হার (SAR)-এর নিরাপত্তা বিধি বজায় রেখে একটি ম্যালিগন্যান্ট টিউমার, হেমোরেজিক স্ট্রোক, এবং ইস্কেমিক স্ট্রোক স্বতন্ত্রভাবে প্রবিষ্ট করানো হয়। এছাড়াও, চিত্র পুনর্গঠনের মধ্য দিয়ে স্পষ্টভাবে ক্ষতটির অবস্থান দৃশ্যায়নের জন্য মনোস্ট্যাটিক রাডার-ভিত্তিক বিলম্ব-এবং-সমষ্টি (DAS) রশ্মি-গঠন বা কনফোকাল মাইক্রোওয়েভ ইমেজিং অ্যালগরিদম উন্নীত করা হয়। সিমুলেশন ফলাফল থেকে এটি প্রকাশিত হয় যে প্রস্তাবিত বো-টাই অ্যান্টেনাটি প্রচলিত প্রতিপক্ষসমূহ হতে উচ্চতর কর্মক্ষমতা অর্জন করে, বিশেষভাবে, ব্যান্ডউইথ এবং বিকিরণ দক্ষতার ব্যাপারে যেখানে প্রস্তাবিত মনোপোল অ্যান্টেনাটি বিশেষত ব্যান্ডউইথ এবং আকৃতির বিষয়ে শ্রেষ্ঠত্ব লাভ করে। স্বাভাবিক সুস্থ টিস্যুর তুলনায় প্রস্তাবিত বো-টাই অ্যান্টেনাটির প্রবাহ ঘনত্ব এবং SAR-এর ব্যাপক বৃদ্ধির দরুন মস্তিষ্কের টিউমারটির সনাক্তকরণ নিশ্চিত করা হয়। অন্য দিকে, সুস্থ মস্তিষ্ক অপেক্ষা প্রস্তাবিত মনোপোল অ্যান্টেনাটির অতিরিক্ত প্রবাহ ঘনত্ব এবং SAR দ্বারা হেমোরেজিক স্ট্রোকটি সনাক্ত করা হয় যদিও ইস্কেমিক স্ট্রোকটির ক্ষেত্রে পরিস্থিতি বিপরীত হয়। পরিশেষে, সংশ্লিষ্ট মাইক্রোওয়েভ চিত্রসমূহ উচ্চ স্থানিক রেজল্যুশন সহকারে দ্বি-মাত্রায় নির্ভরযোগ্যভাবে পুনর্গঠিত করা হয়। অতএব, প্রস্তাবিত গবেষণা কাজটি আগাম এবং দ্রুত রোগ নির্ণয়ের মাধ্যমে মস্তিষ্কের অস্বাভাবিকতা ঘটিত মৃত্যুহার লাঘব করে মানুষের জীবন বাঁচাতে পারে।

ACKNOWLEDGEMENTS

First and foremost, the author expresses her utmost gratitude to Almighty Allah, the Most Praiseworthy and the Most Glorious, for His enormous grace in accomplishing this research work successfully. May Allah's showers of blessings bestow upon His Final Prophet Muhammad (peace be upon him), his family, and his companions.

The author is much obliged to her research supervisor, Major Md Aminul Islam, PhD, Instructor Class B, Department of Electrical, Electronic and Communication Engineering (EECE), Military Institute of Science and Technology (MIST), for his patient guidance, enthusiastic encouragement, and useful critiques of this research work. The author would also like to convey her sincere gratitude to the other faculty members of Department of EECE, MIST, for their invaluable suggestion and inspiration from time to time. Finally, the author extends her heartfelt thanks to her family and friends for their unconditional love and support throughout this research work.

TABLE OF CONTENTS

LIST OF FIGURES

LIST OF TABLES

LIST OF ABBREVIATIONS

Al_2O_3	Alumina ceramic
A/m	Ampere per meter
A/m^2	Ampere per square meter
CER	Ceramic
CSF	Cerebrospinal fluid
CSI	Contrast-source inversion
CST	Computer simulation technology
CT	Computed tomography
DAS	Delay-and-sum
dB	Decibel
DGS	Defected ground structure
EEG	Electro-encephalography
EIT	Electrical impedance tomography
FR	Flame retardant
g	Gram
GHz	Gigahertz
GNI	Gauss-Newton inversion
IFFT	Inverse fast Fourier transform
ISM	Industrial, scientific, and medical
kg/m^3	Kilogram per cubic meter
MATLAB	Matrix laboratory
MEG	Magneto-encephalography
MHz	Megahertz
MIST	Microwave imaging via space-time
MIT	Magnetic induction tomography

mm	Millimeter
mm^3	Cubic millimeter
MRI	Magnetic resonance imaging
m/s	Meter per second
MTS	Metasurface
MWS	Microwave studio
PET	Positron emission tomography
PET	Polyethylene terephthalate
PLA	Polylactic acid
PSMA	Printed square monopole antenna
SAR	Specific absorption rate
S/m	Siemens per meter
TSAR	Tissue sensing adaptive radar
USB	Universal serial bus
UWB	Ultra-wideband
W	Watts
W/kg	Watts per kilogram
2-D	Two-dimensional
3-D	Three-dimensional

LIST OF MAIN SYMBOLS

A_L	Arm length
A_W	Arm width
$A_X(t)$	Averaged signal
c	Velocity of light in vacuum
d	Propagation distance
E_L	Edge-cut length
E_W	Edge-cut width
f	Center frequency
$F(x_i, y_j)$	Grid matrix for phantom region
G_L	DGS ground length
$G(X, Y)$	Grid matrix for scan region
h	Substrate thickness
$HL_{XY}(t)$	Time domain signal with lesion
$H_{XY}(t)$	Time domain signal without lesion
$I(x_i, y_j)$	Intensity values associated with the pixel points
L	Substrate length
$L_{XY}(t)$	Calibrated signal
m	Number of scan positions in a row
M_L	Microstrip feed length
MT	Metal thickness
M_W	Microstrip feed width
n	Number of scan positions in a column
N	Number of propagation medium
N_L	Notch length
N_W	Notch width

P_L	Patch length
P_W	Patch width
$P_{XY}(t)$	Processed signal
S_{11}	Input reflection coefficient
t	Feed-branch length
$tan\delta$	Loss tangent
$t_{XY}(x_i, y_j)$	Round-trip time
w	Hamming window signal
W	Substrate width
ε_r	Relative permittivity
λ	Center wavelength
θ	Polar angle
φ	Azimuth angle

CHAPTER 1
INTRODUCTION

1.1 General

Microwave imaging is a branch of science that utilizes electromagnetic waves in microwave regime, i.e., ~300 MHz - 300 GHz for evaluating hidden or embedded objects in any structure [1]. It is frequently used in medical diagnosis of abnormality or lesion such as tumor, stroke, and so on. In the contemporary world, cancer and stroke have been acknowledged as the second and third leading causes of death respectively [2], [3]. Brain cancer is arguably recognized as the most fatal type of cancer. Statistics reveal that almost 1 % - 2 % of cancer patients in today's world are affected by brain cancer [4]. The rapid accumulation of abnormal cells known as malignant tumor inside the brain accounts for its generation as shown in Fig. 1.1 (a) that is aggressively conducted by the bloodstream or lymph system to the neighboring healthy tissues for overpowering them and generating more tumors [5]. On the contrary, brain stroke is responsible for claiming 1 life in every 6 seconds worldwide [6]. Literally, it is a cerebrovascular accident that brings about sudden obstruction in continuous blood flow containing oxygen and necessary nutrients to the brain, causing loss of neurological function. By and large, there are two broad categories of brain stroke, i.e., hemorrhagic stroke and ischemic stroke as demonstrated in Fig. 1.1 (b). Hemorrhagic stroke occurs when a blood vessel bursts and spills blood into the surrounding brain tissues, interrupting proper functionalities. Conversely, ischemic stroke is caused by the blockage of a blood vessel by a blood clot and thus impeding blood to reach the brain [7]. However, both brain cancer and stroke demand a reliable diagnosis at the early stage before initiating the corresponding treatment owing to the detrimental effects on the most vital organ of the human body.

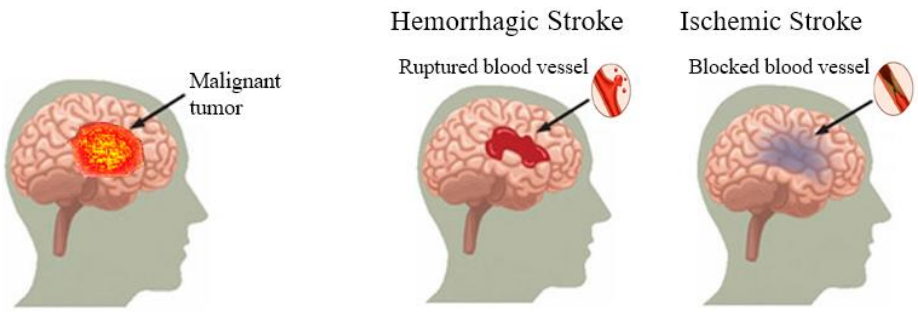

(a) (b)

Fig. 1.1: Abnormalities inside human brain (a) Malignant tumor (b) Types of stroke.

The remainder of this chapter has the following arrangement: Section 1.2 briefly describes the related research works, followed by the motivation of the work in Section 1.3. The proposed research methodology is outlined in Section 1.4. In Section 1.5, the research objectives are included. The research contribution is summarized in Section 1.6. Finally, Section 1.7 represents the research organization.

1.2 Related Works

A thorough review of the related works is carried out for exploring the principal findings and limitations of the existing research. The objectives of the proposed work are set thereby to overcome the research gap and upgrade the performance satisfactorily. During the last two decades, there has been a growing interest in the deployment of microwave imaging for investigating brain abnormalities [8]. Conventionally utilized medical imaging modalities in this respect involve magnetic resonance imaging (MRI) scans, biopsy, X-ray screening, positron emission tomography (PET), computed tomography (CT) scans, electrical impedance tomography (EIT), magnetic induction tomography (MIT), electro-encephalography (EEG), magneto-encephalography (MEG), cerebral angiography, ultra-sound imaging, and so forth [9], [10]. Microwave imaging might become a viable surrogate medical diagnostic technique to the state-of-the-art in light of providing substantial advantages such as safety, portability, low cost, high accuracy, less complexity, promptness, very low power, non-invasive and non-ionizing radiation [11]. Theoretically, the higher the antenna operating frequency, the higher is the spatial resolution of microwave image and the lower is the penetration depth of electromagnetic energy in human tissues. Hence, a trade-off between resolution and penetration prevails. Therefore, a prerequisite for active microwave imaging, particularly the radar-based scheme, is an ultra-wideband (UWB) antenna that covers both low and high-frequency ranges of operation [12]. By definition, an antenna occupying an impedance bandwidth of at least 500 MHz or a fractional bandwidth exceeding 20 % is referred to as a UWB antenna [13]. The typical UWB antennas that are most appealing in this context include monopole antenna, dipole antenna, Vivaldi antenna, bow-tie antenna, pyramidal horn antenna, stacked patch antenna, log-periodic antenna, and spiral antenna [14] as conferred in Table 1.1. Among them, monopole antenna and bow-tie antenna have gained significant momentums on account of certain outstanding criteria such as low fabrication cost, lightweight, and miniature size although monopole antenna suffers from gain limitation while bow-tie antenna suffers from

bandwidth limitation. Currently, a number of research literatures exist on bow-tie antennas for microwave imaging applications [15]-[24]. However, none of these studies focused on the diagnosis of brain abnormalities. Likewise, many research literatures have been published on microwave imaging applications exploiting monopole antennas [25]-[34]. Out of these, only a limited amount emphasized on brain abnormality detection and localization.

Table 1.1: Comparison among suitabilities of UWB antennas employed in microwave imaging [14]

Antenna types	**Bandwidth**	**Gain**	**Cost**	**Weight**	**Size**
Monopole	√	×	√	√	√
Dipole	√	√	×	×	×
Vivaldi	√	×	×	×	×
Bow-tie	×	√	√	√	√
Pyramidal horn	√	√	×	×	×
Stacked patch	√	√	×	×	×
Log periodic	√	√	×	×	×
Spiral	√	√	×	×	×

1.3 Motivation of the Work

From a broader perspective, the motivation of the proposed research work is ascribed to the increased survival rate of humans affected by brain abnormalities via prompt diagnosis and medication. Accordingly, the systematic review of related research works persuades that there is much scope for improvement in the performance metrics of the existing eminent microwave imaging antennas as follows:

(i) Miniaturization of antenna size.

(ii) Widening of antenna bandwidth.

(iii) Augmentation of antenna gain.

(iv) Augmentation of antenna radiation efficiency.

1.4 Research Objectives

Specifically, this research aims to save human lives by mitigating the mortality risk due to brain cancer and stroke through early detection and treatment. On that account, the objectives of this research include:

(i) To propose UWB antennas for the possible detection of lesion inside human phantom.

(ii) To develop a microwave imaging algorithm for lesion image reconstruction inside the phantom.

(iii) To compare the proposed work with existing ones in terms of antenna size, bandwidth, gain, radiation efficiency, image resolution and accuracy.

1.5 Proposed Research Methodology

The methodology for obtaining the expected research outcomes is outlined in the following:

(i) **Software and frequency selection:** The commercial software package computer simulation technology (CST) microwave studio (MWS) is used for antenna and phantom design, simulation and performance analysis while MATLAB is used for lesion image reconstruction. The operating frequency of the antenna is selected within the industrial, scientific, and medical (ISM) band which is used worldwide for biomedical applications [35].

(ii) **Antenna and phantom design:** A non-implantable UWB bow-tie antenna and a monopole antenna are designed within the selected frequency band for the detection and localization of brain tumor and brain stroke respectively. Besides, a multi-layered human head phantom with corresponding lesion is modeled maintaining a minimum gap from the antenna to avoid detrimental side-effects dispersed from antenna radiation.

(iii) **Antenna simulation:** Each antenna is simulated both in free space and with the phantom model in the presence and absence of lesion respectively. By comparing the antenna simulation results with and without lesion over the phantom, the presence of lesion is detected.

(iv) **Biocompatibility analysis:** Along with various performance parameters, the biocompatibility analysis factor represented by specific absorption rate (SAR) is assessed maintaining the IEEE safety level of the human body.

(v) **Implementation of microwave imaging algorithm:** The monostatic radar-based delay-and-sum (DAS) beamforming or confocal microwave imaging algorithm is implemented for the envisaged lesion image reconstruction in two-dimension.

1.6 Research Contribution

In pursuit of fulfilling the distinctive objectives, this research contributes to a number of original developments, some of which are already published in two leading international conferences and the rest are drafted for the possible publications in two reputed journals in the near future. The major contributions of this research are summarized below:

(i) Detection of brain tumor inside a six-layered human head phantom model by designing a self-complementary bow-tie antenna having improved bandwidth and radiation efficiency compared to the existing ones.

(ii) Localization of brain tumor inside the phantom model precisely with a marginal positive error.

(iii) Detection of brain stroke inside a six-layered human head phantom model by designing a defected ground structure (DGS)-based monopole antenna with a trident-shaped feeding strip having improved bandwidth and reduced physical dimension compared to the existing ones.

(iv) Localization of brain stroke inside the phantom model precisely with a marginal negative error.

(v) Foundation for practical detection and localization of brain abnormalities through antenna fabrication with full system measurement in future.

1.7 Research Organization

The research embodied in this thesis is divided into six chapters, organized as follows:

(i) **CHAPTER 1 - INTRODUCTION:** At first, this chapter introduces the general overview. Next, the related works are briefly described, followed by the motivation of the work. Latterly, the research objectives are included. Henceforth, the proposed research methodology is outlined. The research contributions are summarized afterward. Finally, the research organization is represented.

(ii) **CHAPTER 2 - LITERATURE REVIEW:** Initially, the general overview of this chapter is considered. Later on, bow-tie antenna for microwave imaging are explained. Immediately, monopole antenna for microwave imaging are illustrated. In the end, the summary is provided.

(iii) **CHAPTER 3 – THEORETICAL BACKGROUND:** First of all, this chapter represents the general overview. Subsequently, the classification of microwave imaging is dealt with. Later, the microwave imaging algorithms are familiarized.

(iv) **CHAPTER 4 – ANTENNA DESIGN, SIMULATION AND ANALYSIS:** Primarily, the general overview of this chapter is focused. After that, the experimental settings are illuminated. Then, the proposed bow-tie antenna for brain tumor diagnosis is intimated. Succeedingly, the proposed monopole antenna for brain stroke diagnosis is interpreted. Hence, the comparative analysis is presented. At last, the discussion is drawn.

(v) **CHAPTER 5 - CONCLUSION AND FUTURE RECOMMENDATIONS:** Firstly, this chapter sums up the conclusion. Thereafter, the limitations of the work are addressed, followed by the future recommendations.

CHAPTER 2
LITERATURE REVIEW

2.1 General

This chapter considers a comprehensive and in-depth analysis of the existing literature related to the proposed work in support of the related works that is described briefly in Section 1.2 of Chapter 1. The rest of this chapter is oriented as below: In Section 2.2, bow-tie antenna for microwave imaging are explained. Section 2.3 illustrates monopole antenna for microwave imaging. In the end, the summary is provided in Section 2.4.

2.2 Bow-Tie Antenna for Microwave Imaging

Recently, Fiser *et al.* [15] proposed a UWB rounded bow-tie antenna with an overall dimension of 60 × 60 × 50 mm^3 printed on the Rogers-RO4003C substrate for microwave head imaging applications. The layout of this antenna with detailed dimensions of the front view and side view is represented in Fig. 2.1 (a) and Fig. 2.1 (b) sequentially. The simulated bandwidth and radiation efficiency were recorded as 5 GHz and around 80 % respectively.

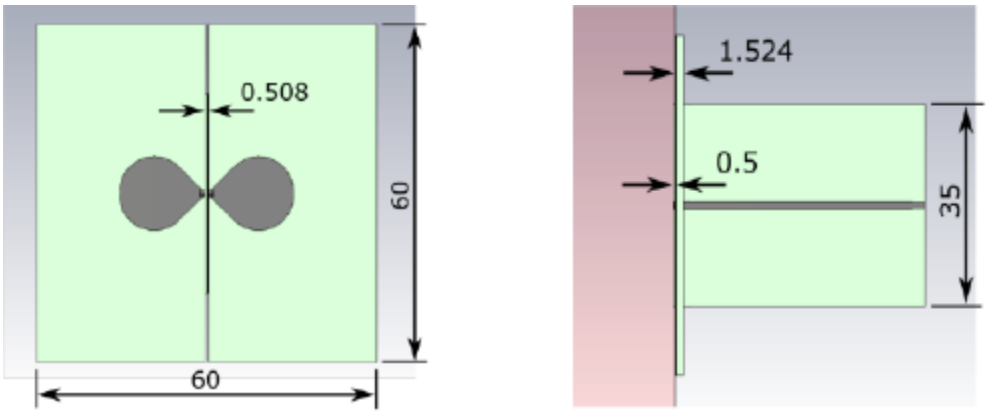

(a) (b)

Fig. 2.1: Layout of the rounded bow-tie antenna on Rogers-RO4003C substrate (a) front view (b) side view (all dimensions are in mm) [15].

In another paper, Rufus *et al.* [16] reported a rounded bow-tie antenna having a compact dimension of 16 × 24 × 1.6 mm^3 fabricated on the FR-4 substrate ($\varepsilon_r = 4.28, tan\delta = 0.001$) for microwave imaging applications. Fig. 2.2 explicates the configuration of this antenna with particular dimensions. The antenna achieved a bandwidth of 0.1 GHz and a gain of approximately 5 dB after simulation.

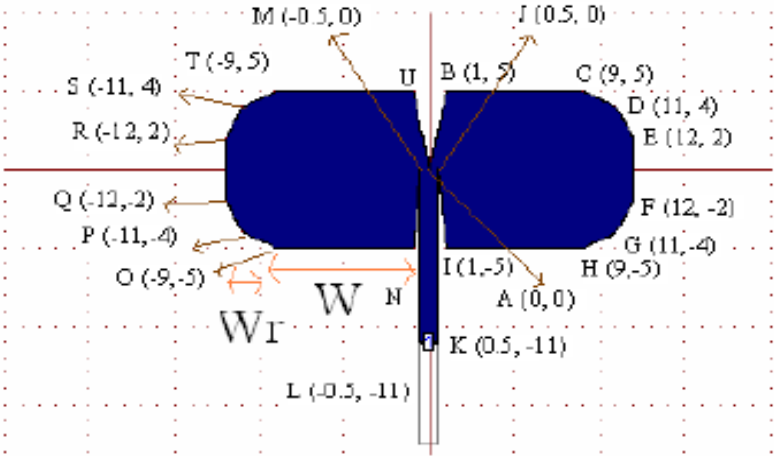

Fig. 2.2: Configuration of the rounded bow-tie antenna on FR-4 substrate (dimensions in mm) [16].

Another UWB compact bow-tie antenna was designed by Hossain *et al.* [17] for cancer detection and treatment. The geometry of this antenna with the top view and bottom view is shown in Fig. 2.3 (a) and Fig. 2.3 (b) correspondingly. The total footprint of the antenna was 34.46 × 23.8 × 1.67 mm^3 embedded on the FR-4 substrate. After simulation, a bandwidth of 0.64 GHz and a radiation efficiency of 75.8 % were obtained.

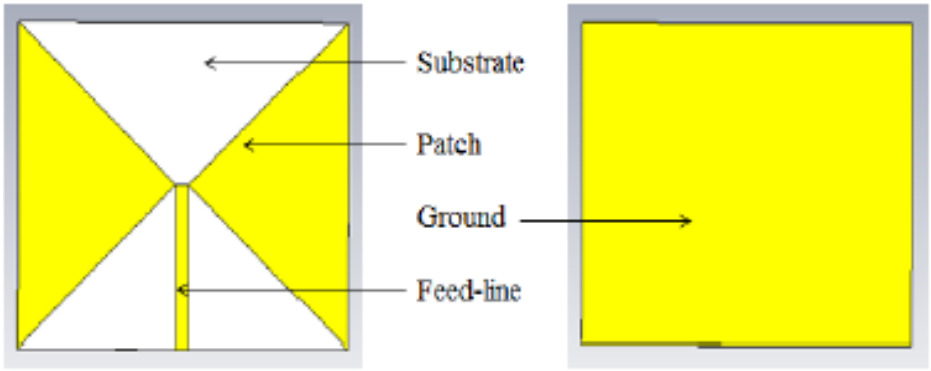

(a) (b)

Fig. 2.3: Geometry of the compact bow-tie antenna on FR-4 substrate (a) top view (b) bottom view [17].

Again, Arayeshnia *et al.* [18] designed and analyzed a UWB meandered bow-tie antenna for wearable microwave brain imaging systems. Fig. 2.4 (a) and Fig. 2.4 (b) depict the prototype of this antenna with specific dimensions of the front view and rear view subsequently. The antenna occupied a size of 18 × 18 × 0.5 mm^3 rooted on the FR-4 substrate ($\varepsilon_r = 4.3$). The simulated bandwidth and radiation efficiency were attained as 3.25 GHz and almost 45 % respectively.

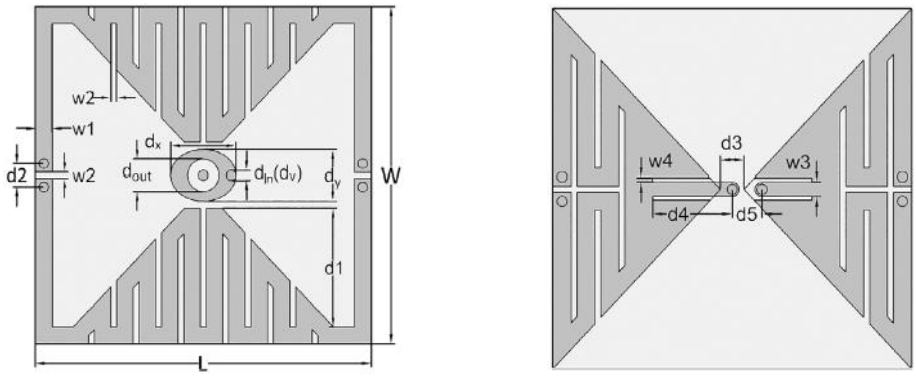

(a) (b)

Fig. 2.4: Prototype of the meandered bow-tie antenna on FR-4 substrate (a) front view (b) rear view ($W = 18$ mm, $L = 18$ mm, $w_1 = 0.9$ mm, $w_2 = 0.3$ mm, $w_3 = 0.7$ mm, $w_4 = 0.2$ mm, $d_1 = 6.4$ mm, $d_2 = 1.2$ mm, $d_3 = 1.2$ mm, $d_4 = 4$ mm, $d_5 = 1.5$ mm, $d_x = 3.5$ mm, $d_y = 2.7$ mm, $d_{out} = 1.68$ mm, $d_{in}(d_v) = 0.51$ mm) [18].

Another paper by Vijayalakshmi *et al.* [19] presented a UWB staircase antipodal bow-tie antenna, occupying a physical dimension of 57 × 30.4 × 1.6 mm^3 integrated on the FR-4 substrate ($\varepsilon_r = 4.4, tan\delta = 0.025$) for microwave imaging applications. The structure of this antenna with detailed dimensions is highlighted in Fig. 2.5. The simulation results revealed that the antenna possessed a bandwidth of 3.17 GHz and a gain of 4.29 dB.

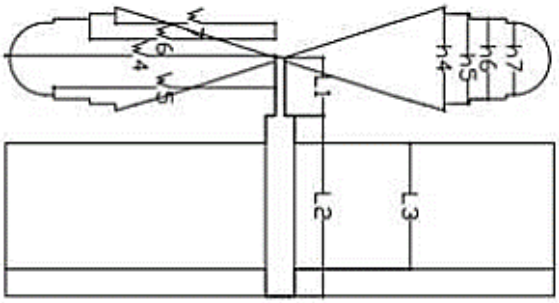

Fig. 2.5: Structure of the staircase antipodal bow-tie antenna on FR-4 substrate ($L_1 = 6$ mm, $L_2 = 18.75$ mm, $L_3 = 13.1$ mm, $w_4 = 28.13$ mm, $w_5 = 22.5$ mm, $w_6 = 18.17$ mm, $w_7 = 16.07$ mm, $h_4 = 18.75$ mm, $h_5 = 15$ mm, $h_6 = 12.5$ mm, $d_7 = 10.74$ mm) [19].

Furthermore, Li *et al.* [20] designed and simulated a UWB double-layered bow-tie antenna for microwave head imaging applications. Fig. 2.6 (a) and Fig. 2.6 (b) specify the configuration of this antenna with the top view and side view chronologically. The antenna was mounted above the Rogers-RT6010 substrate ($\varepsilon_r = 10.2$) having a volume of 30 × 30 × 1.27 mm^3. After simulating the antenna, a bandwidth of 1.5 GHz, a gain of around 6 dB, and a radiation efficiency of nearly 91 % were found.

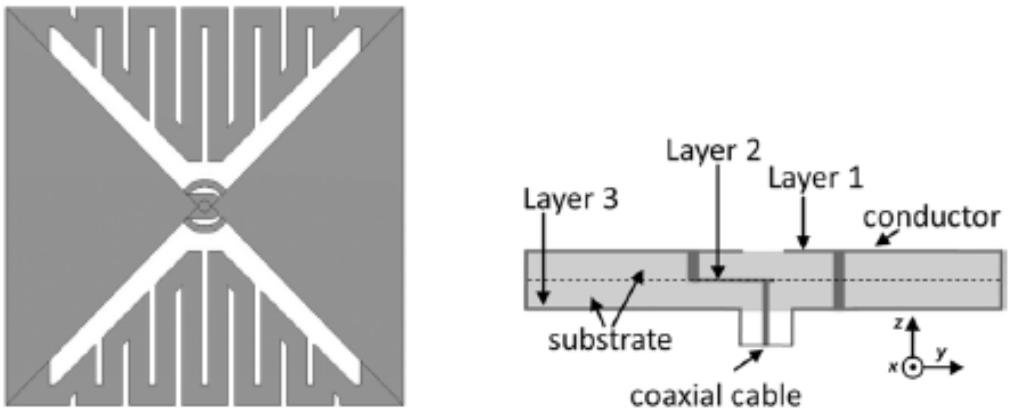

(a) (b)

Fig. 2.6: Configuration of the double-layered bow-tie antenna on Rogers-RT6010 substrate (a) top view (b) side view [20].

The paper of Gomaa *et al.* [21] offered a double-sided triangular bow-tie antenna designed on the Duroid-5880 substrate ($\varepsilon_r = 2.2$) with 37 × 40 × 1.27 mm^3 size for UWB communications. The layout of this antenna is demonstrated in Fig. 2.7. The simulated bandwidth and gain were acquired as 1.8 GHz and 5 dB respectively.

Fig. 2.7: Layout of the double-sided triangular bow-tie antenna on Duroid-5880 substrate [21].

Moreover, Mahalakshmi *et al.* [22] developed a miniaturized hexagonal bow-tie antenna of 10 × 10 × 1 mm^3 volume inlaid on the alumina ceramic (Al_2O_3) substrate ($\varepsilon_r = 9.8$) for biomedical applications. The prototype of this antenna with particular dimensions is pictorialized in Fig. 2.8. The observed values of the simulated bandwidth and gain were around 0.19 GHz and -14.5 dB respectively.

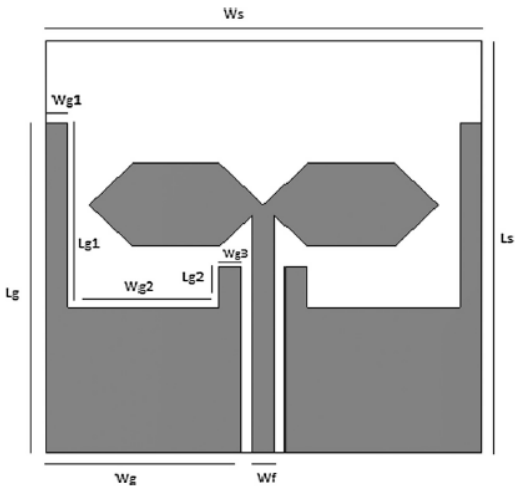

Fig. 2.8: Prototype of the hexagonal bow-tie antenna on Al_2O_3 substrate ($W_s = 10$ mm, $L_s = 10$ mm, $W_g = 4.5$ mm, $L_g = 8$ mm, $W_f = 0.5$ mm, $W_{g1} = 0.5$ mm, $L_{g1} = 4.5$ mm, $W_{g2} = 3.5$ mm, $L_{g2} = 1.5$ mm, $W_{g3} = 0.5$ mm) [22].

In addition, a UWB bow-tie antenna had been implemented by Jalilvand *et al.* [23] for 3-D microwave tomography. Fig. 2.9 displays the geometry of this antenna with specific dimensions. The antenna was manufactured on the Rogers-5880 substrate ($\varepsilon_r = 2.2$) with a volumetric dimension of 22 × 22 × 1.5 mm^3. A bandwidth of 2.4 GHz appeared after performing the simulation.

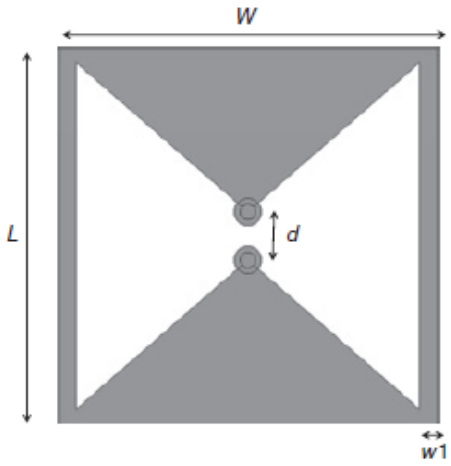

Fig. 2.9: Geometry of the bow-tie antenna on Rogers-5880 substrate ($W = 22$ mm, $L = 22$ mm, $d = 2.8$ mm, $w_1 = 1$ mm) [23].

Also, Aydin *et al.* [24] promoted three bow-tie antennas in their paper for biomedical imaging applications utilizing pure PLA, PLA/copper, and PLA/carbon respectively as substrates. The antenna bandwidth close to 0.2 GHz was the widest for 60 × 60 × 2 mm^3 size implanted on the PLA/copper substrate ($\varepsilon_r = 2.4$). Fig. 2.10 elucidates the structure of this antenna with detailed dimensions.

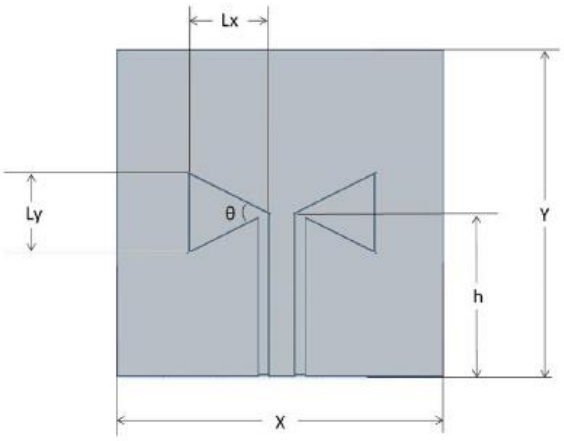

Fig. 2.10: Structure of the bow-tie antenna on PLA/copper substrate ($X = 10$ mm, $Y = 10$ mm, $L_x = 4.5$ mm, $L_y = 8$ mm, $h = 0.5$ mm, $\theta = 53°$) [24].

2.3 Monopole Antenna for Microwave Imaging

In a recent paper, Rahman *et al.* [25] reported a slotted disk monopole antenna occupying $40 \times 38 \times 0.135$ mm^3 dimensions embedded on the PET substrate ($\varepsilon_r = 3.2, tan\delta = 0.022$) for detecting brain stroke. The configuration of this antenna with particular dimensions is explicated in Fig. 2.11. After performing the simulation, a bandwidth of 0.48 GHz, a gain of 2.78 dB, and a radiation efficiency of 99 % were achieved.

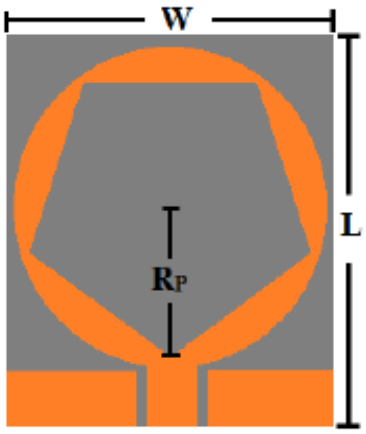

Fig. 2.11: Configuration of the slotted disk monopole antenna on PET substrate ($W = 38$ mm, $L = 40$ mm, $R_P = 16.5$ mm) [25].

Again, Wu *et al.* [26] proposed a UWB semi-circular monopole antenna to locate the position of brain stroke. The total footprint of the antenna was $40 \times 40 \times 0.6$ mm^3 inlaid on the FR-4 substrate ($\varepsilon_r = 4.4, tan\delta = 0.02$). The geometry of this antenna with specific dimensions is depicted in Fig. 2.12. The simulated bandwidth and gain were obtained as 3 GHz and 1.85 dB respectively.

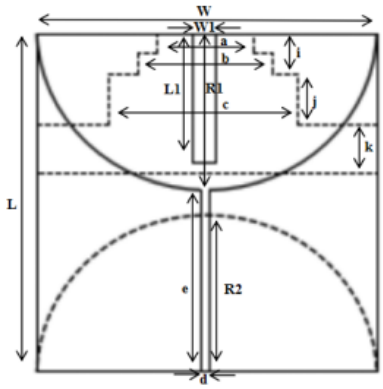

Fig. 2.12: Geometry of the semi-circular monopole antenna on FR-4 substrate ($W = 40$ mm, $L = 40$ mm, $W1 = 18$ mm, $L1 = 0.1$ mm, $R1 = 19.61$ mm, $R2 = 19.61$ mm, $a = 0.6$ mm, $b = 12$ mm, $c = 16$ mm, $d = 20$ mm, $e = 20.39$ mm, $i = 4$ mm, $j = 6$ mm, $k = 8$ mm) [26].

Another paper by Alkasi *et al.* [27] developed a multi-band monopole antenna with an overall dimension of 81 × 45 × 1.6 mm^3 implanted on the FR-4 substrate ($\varepsilon_r = 4.3$) for microwave imaging applications. The prototype of this antenna with detailed dimensions of the front view and back view is specified in Fig. 2.13 (a) and Fig. 2.13 (b) successively. The widest bandwidth after executing the simulation was recorded as 0.23 GHz for the resonant frequency of 2.75 GHz.

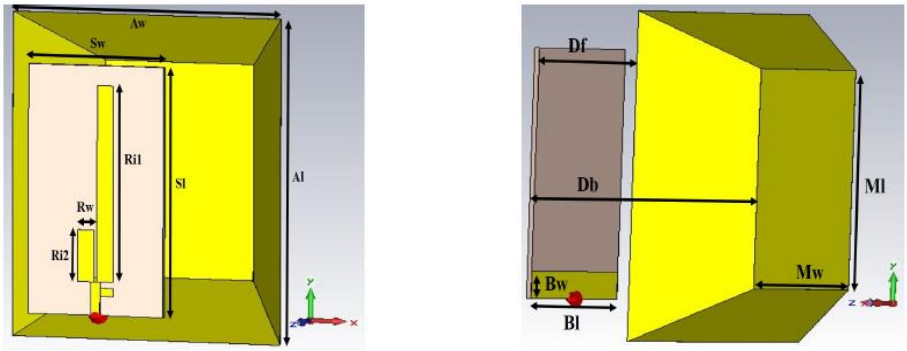

(a) (b)

Fig. 2.13: Prototype of the multi-band monopole antenna with reflector on FR-4 substrate (a) front view (b) back view ($Sw = 45$ mm, $Sl = 81$ mm, $Ri1 = 72$ mm, $Ri2 = 19$ mm, $Rw = 5.363$ mm, $Aw = 90$ mm, $Al = 120$ mm, $Df = 50$ mm, $Db = 80$ mm, $Bw = 10$ mm, $Bl = 45$ mm, $Mw = 50$ mm, $Ml = 80$ mm) [27].

Moreover, Hossain *et al.* [28] in their paper designed and optimized a UWB monopole antenna with a two-branch feeding strip to diagnose brain stroke. Fig. 2.14 (a) and Fig. 2.14 (b) show the layout of this antenna with particular dimensions of the top view and bottom view consecutively. The antenna had a volume of 30 × 20 × 1.5 mm^3 printed on the Rogers-

RO3003 substrate ($\varepsilon_r = 3, tan\delta = 0.001$). The simulated bandwidth, gain, and radiation efficiency were attained as 3.85 GHz, 2.05 dB, and 78.76 % respectively.

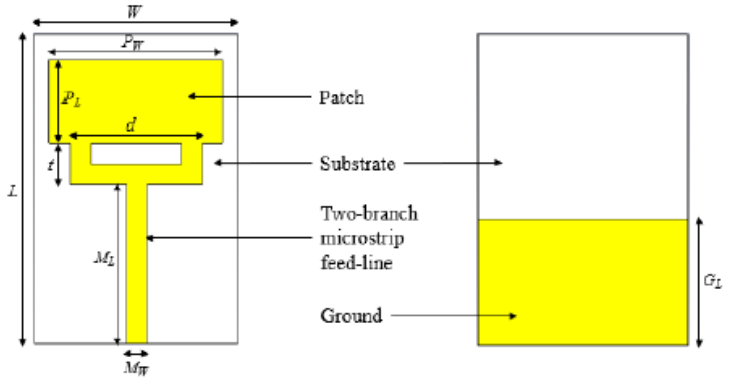

(a) (b)

Fig. 2.14: Layout of the two-branch fed monopole antenna on Rogers-RO3003 substrate (a) top view (b) bottom view ($W = 20$ mm, $L = 30$ mm, $P_W = 17$ mm, $P_L = 8$ mm, $d = 13$ mm, $t = 4$ mm, $M_W = 2$ mm, $M_L = 15.5$ mm, $G_L = 12.2$ mm) [28].

A UWB folded strip monopole antenna with a size of 40 × 32 × 0.8 mm^3 integrated on the FR-4 epoxy substrate ($\varepsilon_r = 4.4, tan\delta = 0.02$) was introduced by Bhardwaj *et al.* [29] for brain stroke detection. The structure of this antenna with specific dimensions is displayed in Fig. 2.15. From the simulation results, the antenna acquired a bandwidth of 3.28 GHz and a gain of 6.8 dB.

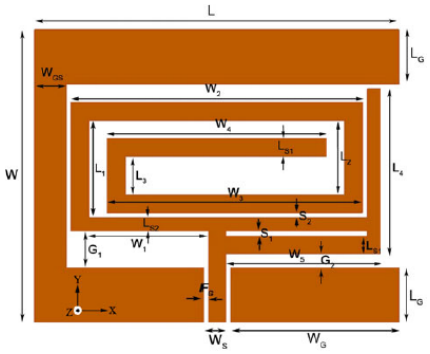

Fig. 2.15: Structure of the folded strip monopole antenna on FR-4 epoxy substrate ($W = 32$ mm, $L = 40$ mm, $L_1 = 10.5$ mm, $L_2 = 8$ mm, $L_3 = 4$ mm, $L_4 = 18$ mm, $W_1 = 15$ mm, $W_2 = 32$ mm, $W_3 = 28$ mm, $W_4 = 24$ mm, $W_5 = 17$ mm, $L_{S1} = 2$ mm, $L_{S2} = 0.5$ mm, $F_G = 0.5$ mm, $L_G = 6$ mm, $W_G = 18.5$ mm, $W_S = 2$ mm, $W_{GS} = 3.5$ mm, $S_1 = 0.5$ mm, $S_2 = 0.5$ mm, $G_1 = 4$ mm, $G_2 = 1.5$ mm) [29].

Another UWB flexible monopole antenna was implemented by Bashri *et al.* [30] for a wearable head imaging system. Fig. 2.16 (a) and Fig. 2.16 (b) pictorialize the geometry of

this antenna with detailed dimensions of the top view and bottom view accordingly. The antenna was mounted above the PET substrate ($\varepsilon_r = 2.4$) having a volumetric dimension of 70 × 30 × 0.075 mm^3 and the simulated bandwidth appeared as 2.2 GHz.

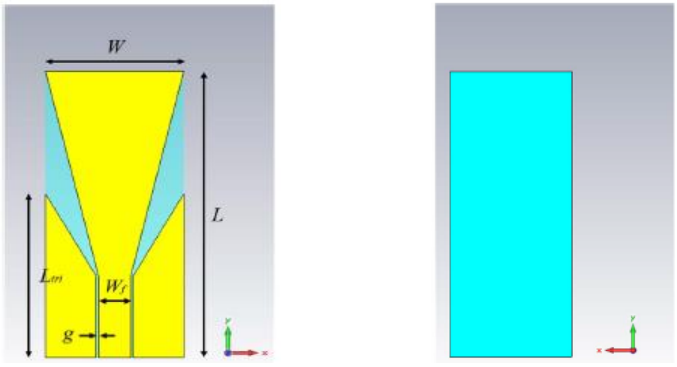

(a) (b)

Fig. 2.16: Geometry of the flexible monopole antenna on PET substrate (a) top view (b) bottom view ($W = 30$ mm, $L = 70$ mm, $g = 0.5$ mm, $W_f = 7$ mm, $L_{tri} = 44$ mm) [30].

Furthermore, Talukder *et al.* [31] presented a UWB monopole antenna capturing 70 × 60 × 1.5 mm^3 size fabricated on the FR-4 substrate ($\varepsilon_r = 4.4$) for microwave head imaging applications. The configuration of this antenna with particular dimensions of the front view and back view is elucidated in Fig. 2.17 (a) and Fig. 2.17 (b) in succession. The simulation results manifested that the antenna possessed a bandwidth of 2.37 GHz, a gain of 5.95 dB, and a radiation efficiency of 93 %.

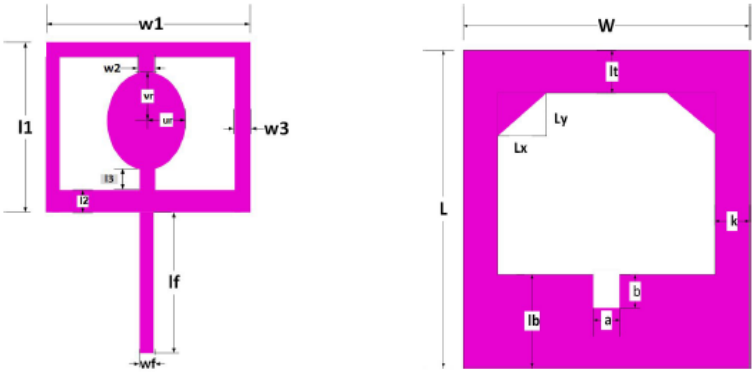

(a) (b)

Fig. 2.17: Configuration of the monopole antenna on FR-4 substrate (a) front view (b) back view ($W = 60$ mm, $L = 70$ mm, $w1 = 30$ mm, $w2 = 2.9$ mm, $w3 = 2$ mm, $wf = 2.72$ mm, $l1 = 25$ mm, $l2 = 4$ mm, $l3 = 2$ mm, $lf = 21.5$ mm, $ur = 7$ mm, $vr = 9$ mm, $Lx = 6$ mm, $Ly = 6$ mm, $lt = 6$ mm, $lb = 19.5$ mm, $k = 5$ mm, $a = 3.1$ mm, $b = 4$ mm) [31].

In another paper, Vasquez *et al.* [32] designed and experimentally assessed a UWB monopole antenna to localize brain stroke. Fig. 2.18 (a) and Fig. 2.18 (b) represent the prototype of this antenna with specific dimensions of the top view and bottom view distinctively. The antenna had a physical dimension of 38 × 30 × 1.6 mm^3 manufactured on the FR-4 substrate. The simulated bandwidth was observed as nearly 1.22 GHz.

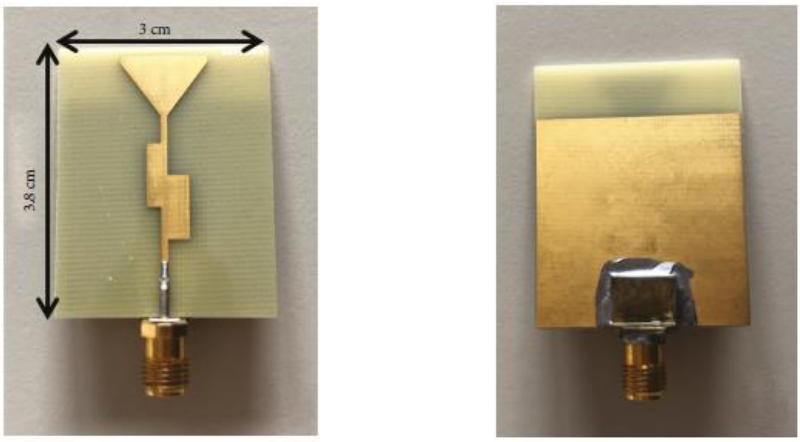

(a) (b)

Fig. 2.18: Prototype of the monopole antenna on FR-4 substrate (a) top view (b) bottom view [32].

Also, Mobashsher *et al.* [33] promoted a UWB monopole antenna with a volume of 80 × 45 × 15 mm^3 designed on the FR-4 substrate ($\varepsilon_r = 4.5, tan\delta = 0.02$) for locating hemorrhagic stroke. The structure of this antenna with detailed dimensions is highlighted in Fig. 2.19. The antenna exhibited 1.15 GHz bandwidth and 3.5 dB gain after simulation.

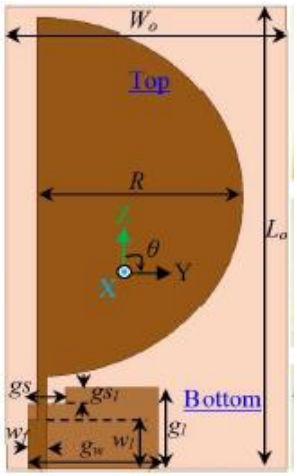

Fig. 2.19: Structure of the monopole antenna on FR-4 substrate ($W_o = 45$ mm, $L_o = 80$ mm, $R = 32$ mm, $w_i = 9$ mm, $w_f = 3$ mm, $g_i = 15$ mm, $g_w = 21$ mm, $gs_i = 3$ mm, $gs = 6$ mm) [33].

In addition, Razzicchia *et al.* [34] offered a metasurface (MTS)-enhanced printed square monopole antenna (PSMA) for detecting and localizing both hemorrhagic and ischemic strokes. Fig. 2.20 (a) and Fig. 2.20 (b) demonstrate the layout of the PSMA with particular dimensions and PSMA with MTS superstrate loading respectively. The antenna was rooted on the RT/duroid-5880 LZ substrate ($\varepsilon_r = 1.96, tan\delta = 0.0019$) having a size of 76 × 38 × 1.026 mm^3. The simulated bandwidth was found as approximately 0.3 GHz.

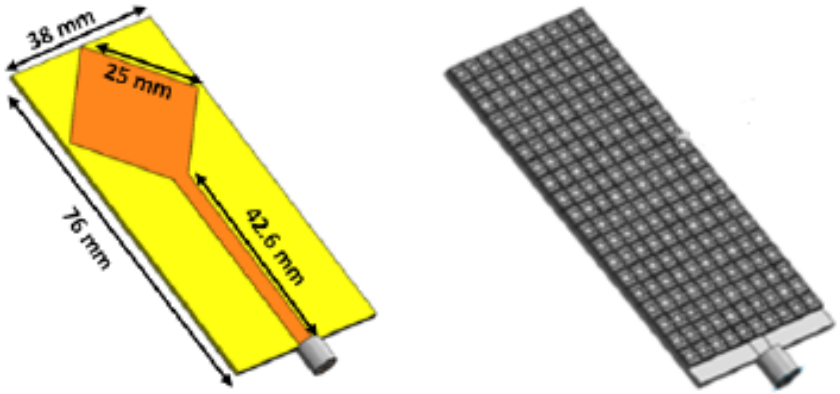

(a) (b)

Fig. 2.20: Layout of the monopole antenna on RT/duroid-5880 LZ substrate (a) PSMA (b) PSMA with MTS superstrate loading [34].

2.4 Summary

In this chapter, the most remarkable bow-tie antenna and monopole antenna for microwave imaging are studied in detail. However, it comes to light that the antennas exerted in these literatures suffered from bulky size, narrow bandwidth, poor gain, and poor radiation efficiency. As a consequence, the resolution and accuracy of the microwave images were not up to the mark. Therefore, more research is mandatory to enrich the performance further across all ramifications.

CHAPTER 3
THEORETICAL BACKGROUND

3.1 General

In this chapter, a vivid concept of the theoretical background is represented which is the primary need to carry out a successful research work. The remainder of this chapter has the following organization: Section 3.2 deals with the classification of microwave imaging, especially active microwave imaging. In Section 3.3, the microwave imaging algorithms are familiarized with an elaboration of the monostatic radar-based confocal algorithm.

3.2 Classification of Microwave Imaging

Microwave imaging is generally classified into three major groups, i.e., passive microwave imaging, hybrid or thermo-acoustic microwave imaging, and active microwave imaging as seen in Fig. 3.1. Nevertheless, active microwave imaging is further classified into two types, i.e., microwave tomography and radar-based microwave imaging [36]. In the passive microwave imaging approach, the presence of a lesion is detected by measuring the temperature difference between healthy tissue and unhealthy tissue exploiting a radiometry device as the prime element. In contrast, the hybrid or thermo-acoustic microwave imaging method utilizes microwave sensors and ultrasonic transducers to evaluate the variations of pressure waves between injured tissue and uninjured tissue for lesion diagnosis. However, active microwave imaging is the most prominent technique that exploits an antenna as the core element to detect the existence of the lesion by assessing the huge contrast between the dielectric properties of normal tissue and abnormal tissue [37].

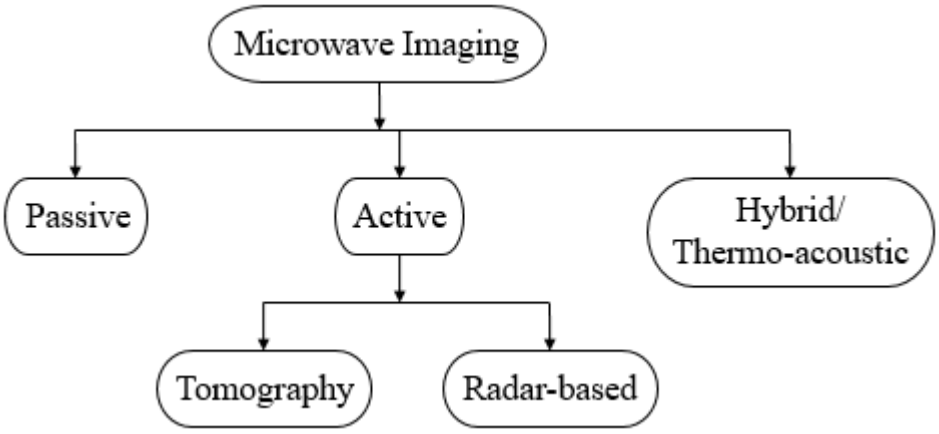

Fig. 3.1: Classification of microwave imaging.

3.2.1 Active Microwave Imaging

More specifically, in the active microwave imaging technique, the setup for brain abnormality detection with localization consists of four parts - a transmitter antenna, a receiver antenna, a head phantom, and a signal storing and processing unit [38], [39] as depicted in Fig. 3.2. The microwave signal originated by the transmitter antenna propagates through air to the head phantom and then back-scattered towards the receiver antenna. The received signal is characterized by three parts - the directly coupled signal from the transmitter antenna, the reflected signal from various layers of the head phantom (i.e., skin, fat, bone, brain, etc.), and lesion reflection. Location pertinent to the lesion acquires higher energy level (i.e., current density, SAR, etc.) than normal healthy tissue [40]. Thus, the presence of a lesion might be detected. However, with a view to reconstructing the image of the lesion for an explicit visualization of its location, the phantom is mechanically rotated along its axis by minimal angle steps in order that it can be sequentially scanned by the transmitter antenna for numerous positions [41]. The signal storing and processing unit further applies suitable microwave imaging algorithms to the received antenna scattering parameters for the generation of microwave images.

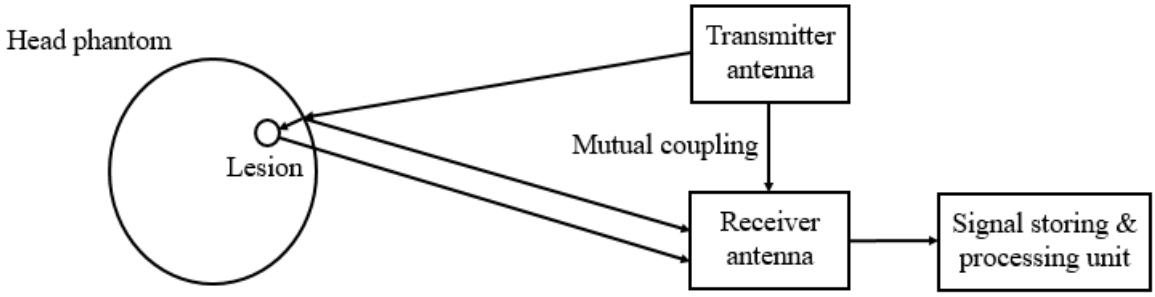

Fig. 3.2: Schematic diagram of active microwave imaging-based brain abnormality detection and localization.

3.3 Microwave Imaging Algorithms

The microwave tomography scheme reproduces the dielectric properties (i.e., relative permittivity and conductivity) of the lesion from the received scattered waves by implementing an inverse non-linear scattering algorithm, for example, Gauss-Newton inversion (GNI) algorithm, contrast-source inversion (CSI) algorithm, and so on [42]. Such a scheme is more complicated due to the requirement of large mathematical operators. Contrarily, in the radar-based microwave imaging scheme, the center position of the lesion

is concentrated by virtue of strong reflection. This scheme is more preferable because of involving a less sophisticated linear scattering algorithm, for instance, delay-and-sum (DAS) beamforming or confocal microwave imaging algorithm, microwave imaging via space-time (MIST) beamforming algorithm, tissue sensing adaptive radar (TSAR) algorithm, and so forth [43].

3.3.1 Monostatic Radar-Based Confocal Algorithm

The monostatic radar-based delay-and-sum (DAS) beamforming or confocal microwave imaging algorithm is one of the most promising algorithms which has widespread use in lesion image reconstruction [44]. The flowchart of this algorithm is pictorialized in Fig. 3.3. The algorithm with each step is thoroughly described below:

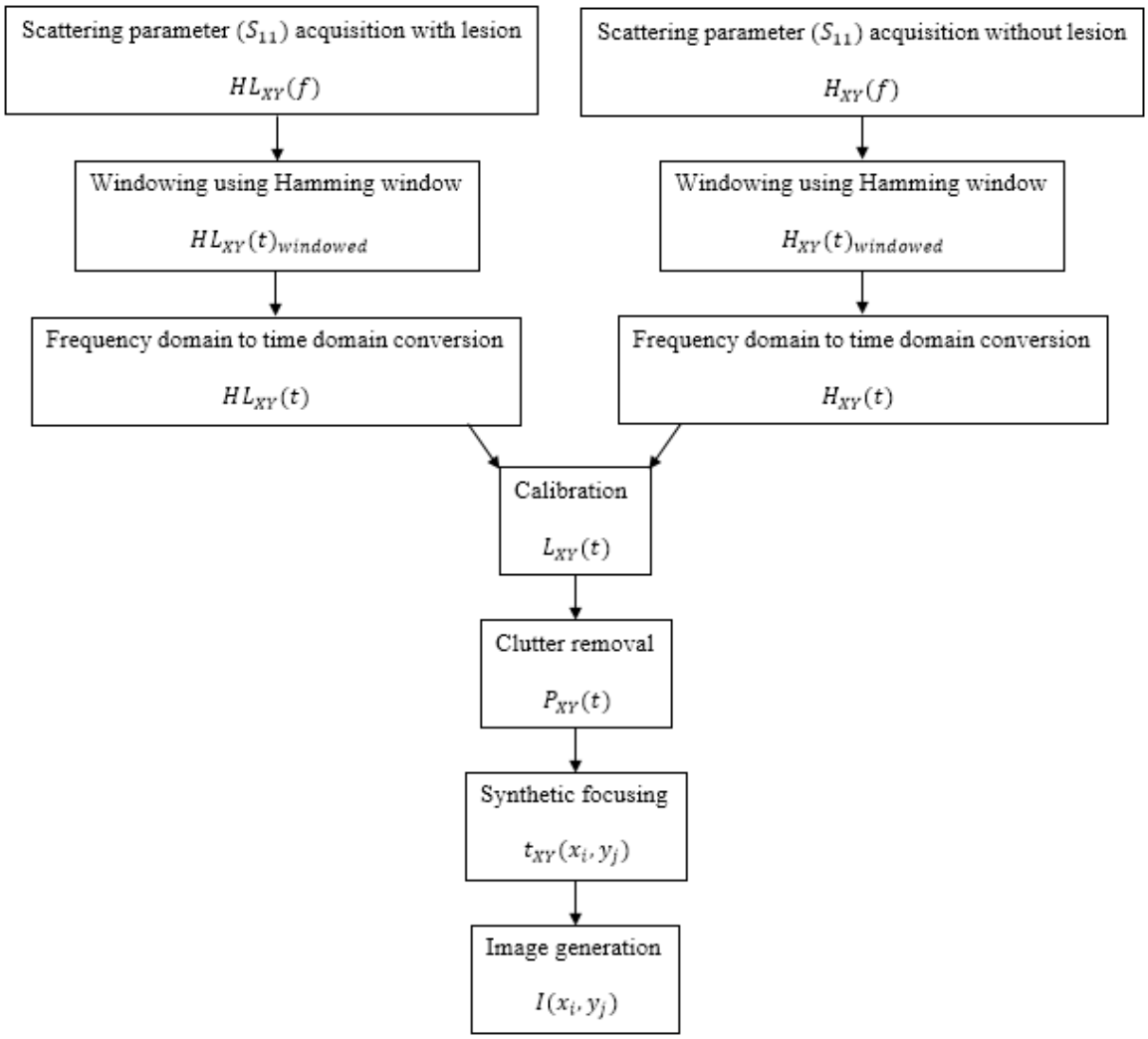

Fig. 3.3: Monostatic radar-based delay-and-sum (DAS) beamforming or confocal microwave imaging algorithm for lesion image reconstruction.

(i) **Scattering parameter (S_{11}) acquisition:** At first, the rotation of the phantom is executed mechanically along its axis with the least possible angle steps so that the antenna can scan the phantom in a sequential manner for miscellaneous positions. The scan region is allocated in an $(m \times n)$ grid that can be represented by the following matrix:

$$G(X,Y) = \begin{bmatrix} (1,1) & (1,2) & \cdots & (1,n) \\ (2,1) & (2,2) & \cdots & (2,n) \\ (3,1) & (3,2) & \cdots & (3,n) \\ \vdots & \vdots & \ddots & \vdots \\ (m,1) & (m,2) & \cdots & (m,n) \end{bmatrix} \quad (3.1)$$

Since the single antenna acts as a transceiver in the monostatic approach, therefore, it radiates UWB microwave pulse that is circulated via air to the layers of the phantom in the presence and absence of lesion respectively and after that is reflected back towards the same antenna [45]. At each scan position, a huge number of scattering parameters (S_{11}) with lesion $HL_{XY}(f)$ and without lesion $H_{XY}(f)$ are recorded over the predetermined UWB frequency range.

(ii) **Windowing using Hamming window:** The acquired scattering parameters (S_{11}) with lesion $HL_{XY}(f)$ and without lesion $H_{XY}(f)$ are windowed using the Hamming window to reduce the side lobe levels as follows:

$$HL_{XY}(f)_{windowed} = HL_{XY}(f) * w \quad (3.2)$$

$$H_{XY}(f)_{windowed} = H_{XY}(f) * w \quad (3.3)$$

Where, w = Hamming window signal.

(iii) **Frequency domain to time domain conversion:** The windowed signals with lesion $HL_{XY}(f)_{windowed}$ and without lesion $H_{XY}(f)_{windowed}$ are converted from the frequency domain to the equivalent time domain by taking their respective inverse fast Fourier transform (IFFT) as expressed below:

$$HL_{XY}(t) = IFFT(HL_{XY}(f)_{windowed}) \quad (3.4)$$

$$H_{XY}(t) = IFFT(H_{XY}(f)_{windowed}) \quad (3.5)$$

(iv) **Calibration:** The time domain signal without lesion $H_{XY}(t)$ is subtracted from that with lesion $HL_{XY}(t)$ to extract the lesion response in the time domain referred to as the calibrated signal given in the following equation:

$$L_{XY}(t) = HL_{XY}(t) - H_{XY}(t) \tag{3.6}$$

(v) **Clutter removal:** The calibrated signal $L_{XY}(t)$ still contains clutter or unwanted reflections dominated by the antenna and the environment. In order to remove this clutter, the calibrated signal $L_{XY}(t)$ is first averaged by adding it in a given row of grid $(m \times n)$ and then dividing it with the total number of scan positions in that row as derived below:

$$A_X(t) = \frac{\sum_{Y=1}^{m} L_{XY}(t)}{m} \tag{3.7}$$

Hence,

$$A_X(t) = \begin{bmatrix} A_1(t) \\ A_2(t) \\ A_3(t) \\ \vdots \\ A_m(t) \end{bmatrix} \tag{3.8}$$

The resultant averaged signal $A_X(t)$ is then deducted from the calibrated signal $L_{XY}(t)$ known as the processed signal conferred in the following expression:

$$P_{XY}(t) = L_{XY}(t) - A_X(t) \tag{3.9}$$

Consequently,

$$P_{XY}(t) = \begin{bmatrix} P_{11}(t) & P_{12}(t) & \cdots & P_{1n}(t) \\ P_{21}(t) & P_{22}(t) & \cdots & P_{2n}(t) \\ P_{31}(t) & P_{32}(t) & \cdots & P_{3n}(t) \\ \vdots & \vdots & \ddots & \vdots \\ P_{m1}(t) & P_{m2}(t) & \cdots & P_{mn}(t) \end{bmatrix} \tag{3.10}$$

(vi) **Synthetic focusing:** The round-trip time is computed aiming to perform the synthetic focusing. For the purpose of computing the round-trip time, firstly, the phantom region is divided in a grid like structure $F(x_i, y_j)$ consisting of focal points

or pixel points. The distance between each scan position (X, Y) and focal point (x_i, y_j) is calculated as follows:

$$D = \sqrt{(X - x_i)^2 + (Y - y_j)^2} \tag{3.11}$$

The propagation distance (d) for each of the N media is evaluated and transformed to round-trip time (t) based on the average wave speed $(c/\sqrt{\varepsilon_r})$ afterward. Hence, the total round-trip time is deduced from the following equations:

$$t_{XY}(x_i, y_j) = t_{(M1)} + t_{(M2)} + \cdots + t_{(MN)} \tag{3.12}$$

$$t_{XY}(x_i, y_j) = \frac{2d_{(M1)}}{c/\sqrt{\varepsilon_{r(M1)}}} + \frac{2d_{(M2)}}{c/\sqrt{\varepsilon_{r(M2)}}} + \cdots + \frac{2d_{(MN)}}{c/\sqrt{\varepsilon_{r(MN)}}} \tag{3.13}$$

Where, $c =$ velocity of light in vacuum $= 3 \times 10^8$ m/s; $\varepsilon_r =$ relative permittivity of the propagation medium.

(vii) **Image generation:** The processed signal $P_{XY}(t)$ at the round-trip time $t_{XY}(x_i, y_j)$ is estimated as follows attempting to generate the intensity values associated with the pixel points:

$$I(x_i, y_j) = \left[\sum_{X=1}^{m} \sum_{Y=1}^{n} P_{XY}\left(t_{XY}(x_i, y_j)\right)\right]^4 \tag{3.14}$$

CHAPTER 4
ANTENNA DESIGN, SIMULATION AND ANALYSIS

4.1 General

This chapter focuses on the design, simulation, and analysis of two different types of ultra-wideband (UWB) antennas, i.e., a self-complementary bow-tie antenna and a defected ground structure (DGS)-based monopole antenna with a trident-shaped feeding strip intended to diagnose a brain tumor and a brain stroke respectively inside a six-layered human head phantom model. The rest of this chapter is arranged as follows: In Section 4.2, the experimental settings are illuminated. Section 4.3 intimates the proposed bow-tie antenna for brain tumor diagnosis showcasing antenna geometry, antenna design equations, simulation results in free space, antenna with biological tissue model, and simulation results with biological tissue model for the detection and localization of brain tumor. The proposed monopole antenna for brain stroke diagnosis assimilating antenna geometry, antenna design equations, antenna design evolution, simulation results in free space, antenna with biological tissue model, and simulation results with biological tissue model for the detection and localization of brain stroke is interpreted in Section 4.4. Section 4.5 presents the comparative analysis constituting the comparison with existing bow-tie antennas and monopole antennas. At last, the discussion is drawn in Section 4.6.

4.2 Experimental Settings

The proposed scenario under the experimental settings of monostatic radar-based microwave head imaging system for brain abnormality detection and localization is displayed in Fig. 4.1. Here, an anatomically realistic 3-D human head phantom is mounted on a horizontal rotating platform that is controlled by a stepper motor. The antenna fixed by an adjustable holder is connected to a microwave sensor through a universal serial bus (USB) cable which is further connected to a laptop through another USB cable. At each scanning angle of rotation, the antenna transmits UWB pulse generated by the microwave sensor to the head phantom in the presence and absence of the intracranial brain injury respectively. The reflected or scattered waves are received by the same antenna and then sent to the laptop via the microwave sensor for storing and post-processing.

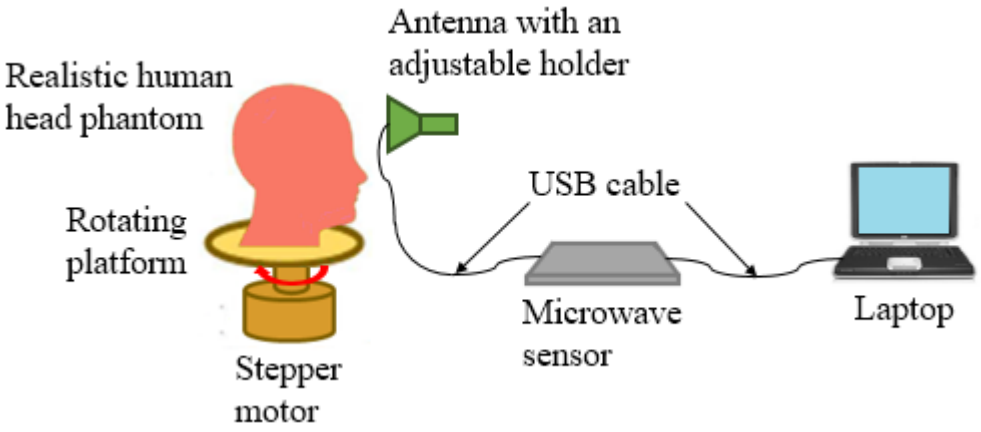

Fig. 4.1: Experimental settings of monostatic radar-based microwave head imaging system for brain abnormality detection and localization.

4.3 Proposed Bow-Tie Antenna for Brain Tumor Diagnosis

4.3.1 Antenna Geometry

Fig. 4.2 shows the detailed geometry of the proposed bow-tie antenna while Table 4.1 enlists its optimum dimensions from which the design equations are deduced. The antenna is structurally planar and rectangular with an overall volume of 27 × 17 × 0.787 mm^3. Commercially available dielectric material Rogers-RT5880 with relative permittivity, $\varepsilon_r = 2.2$, loss tangent, $tan\delta = 0.0009$, and thickness, $h = 0.787$ mm is selected as the substrate while annealed copper with thickness, $MT = 0.035$ mm is selected as the metal.

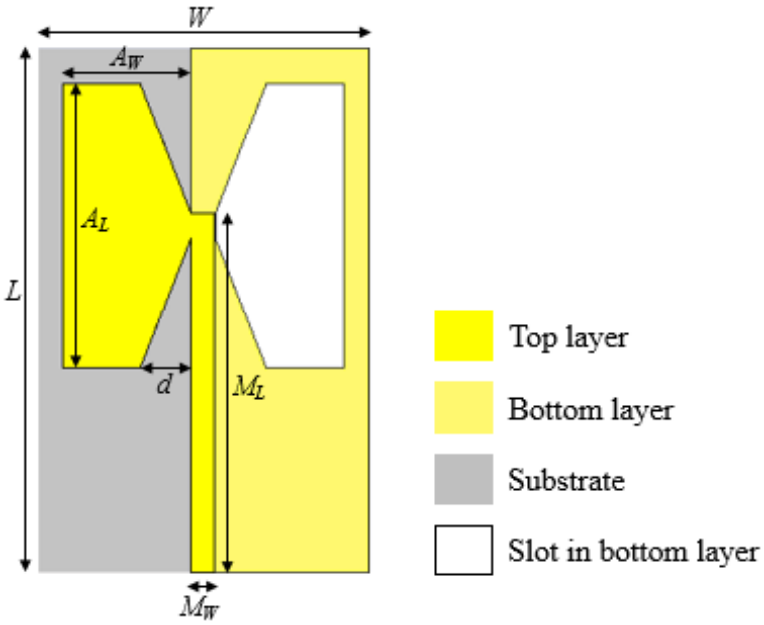

Fig. 4.2: Geometry of the proposed bow-tie antenna.

Table 4.1: Optimum dimensions of the proposed bow-tie antenna

Antenna parameters	Symbol	Value (mm)
Substrate width	W	17
Substrate length	L	27
Substrate thickness	h	0.787
Metal thickness	MT	0.035
Arm width	A_W	6.55
Arm length	A_L	14.7
Microstrip feed width	M_W	1.3
Microstrip feed length	M_L	18.5
Feed to flare region distance	d	2.6

A polygonal radiating metal arm integrated with a 50 Ω microstrip feed-line is etched on the top layer of the substrate whereas the bottom layer comprises of a partial metal ground plane. Moreover, a complementary slot of the radiating arm is inserted on the ground plane, yielding a self-complementary bow-tie antenna. The input impedance of the antenna is matched with the feed-line impedance by optimizing its design parameters effectively through the iterative simulation method.

4.3.2 Antenna Design Equations

(i) **Arm width (A_W):** The arm width (A_W) is determined from the following equation:

$$A_W = \frac{\lambda}{7.63} \tag{4.1}$$

Where, λ = center wavelength = c/f; c = velocity of light in vacuum = 3×10^8 m/s; f = center frequency.

(ii) **Arm length (A_L):** The arm length (A_L) can be formulated as follows:

$$A_L = \frac{\lambda}{3.4} \tag{4.2}$$

(iii) **Substrate width (W):** The substrate width (W) is obtained from the following expression:

$$W = A_W + 13h \tag{4.3}$$

Where, h = substrate thickness.

(iv) **Substrate length (L):** The substrate length (L) is derived as below:

$$L = A_L + 16h \tag{4.4}$$

4.3.3 Simulation Results in Free Space

The proposed bow-tie antenna is designed and simulated in computer simulation technology (CST) microwave studio (MWS), a commercially available full-wave electromagnetic software package based on finite integration technique. After performing antenna simulation in free space, the following results are attained:

Fig. 4.3 represents the simulated S_{11} parameter of the proposed bow-tie antenna in free space. It is obvious that the antenna resonates at the frequency of 6.37 GHz with a small reflection coefficient of -53.84 dB due to a good impedance matching. Moreover, the antenna achieves an ultra-wide impedance bandwidth of 5.14 GHz (5.89 GHz - 11.03 GHz) for $|S_{11}| \leq -10$ dB which is the prime need for microwave imaging-based brain tumor detection.

The radiation efficiency of the proposed bow-tie antenna after simulation in free space is demonstrated in Fig. 4.4. Verily, the antenna possesses an extensive radiation efficiency of 0.9687, i.e., 96.87 % at 6.37 GHz resonant frequency.

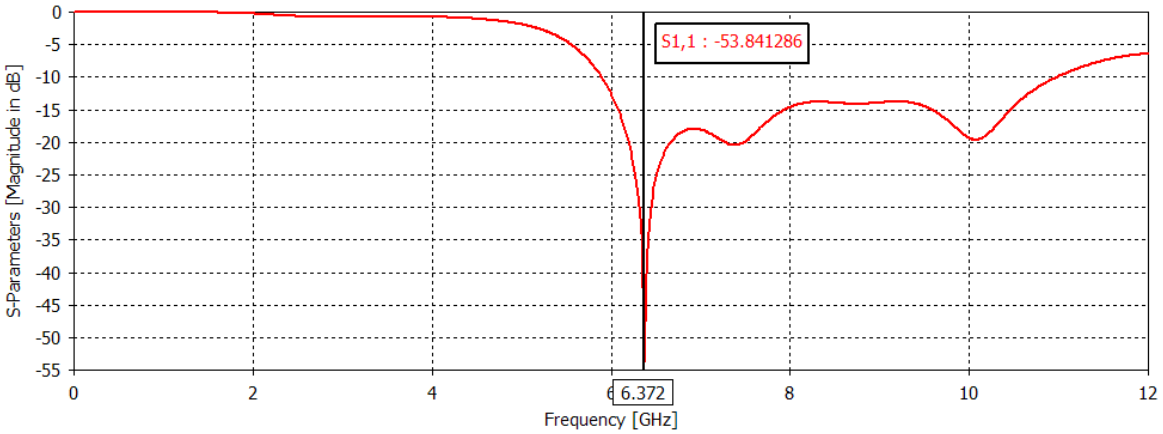

Fig. 4.3: Simulated reflection coefficient (S_{11}) of the proposed bow-tie antenna in free space.

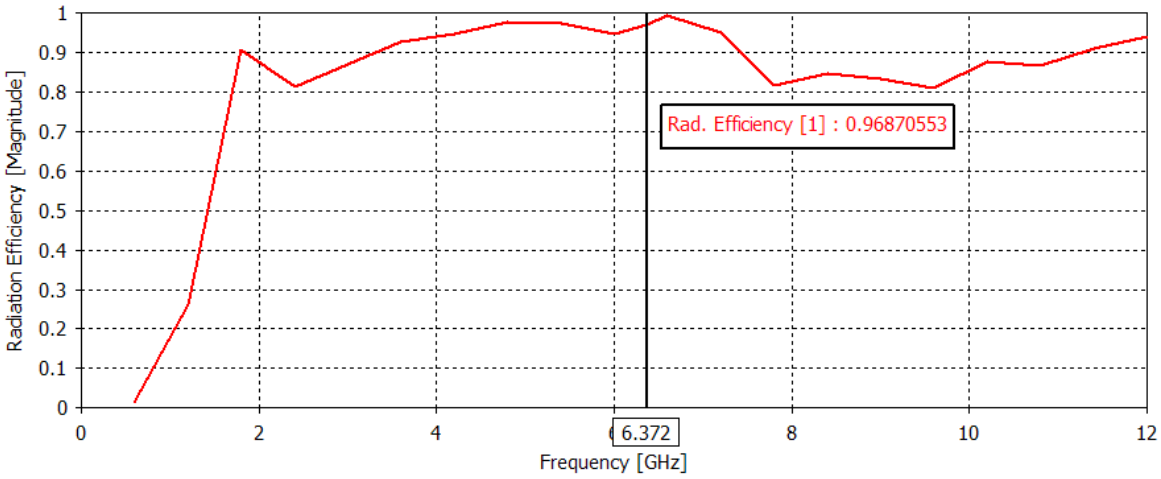

Fig. 4.4: Simulated radiation efficiency of the proposed bow-tie antenna in free space.

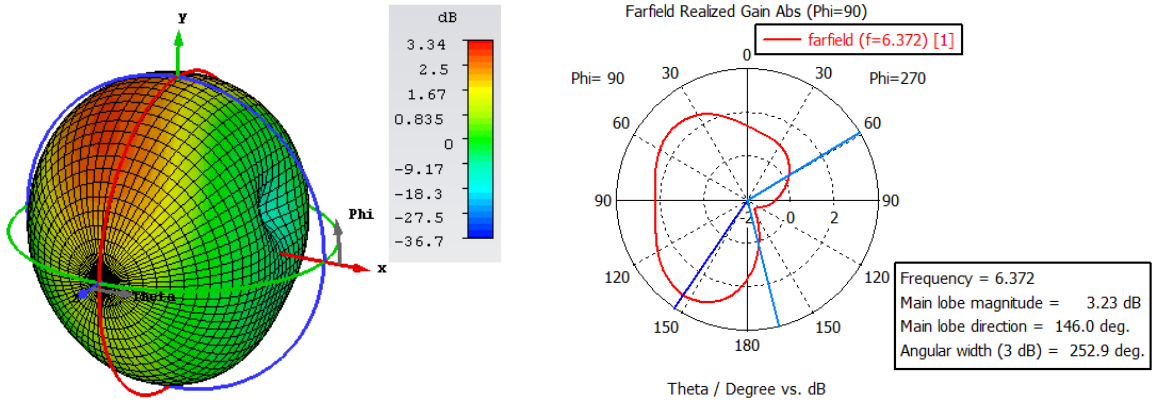

(a) (b)

Fig. 4.5: Simulated far-field gain pattern of the proposed bow-tie antenna in free space at resonant frequency (a) 3-D view (b) 2-D polar view.

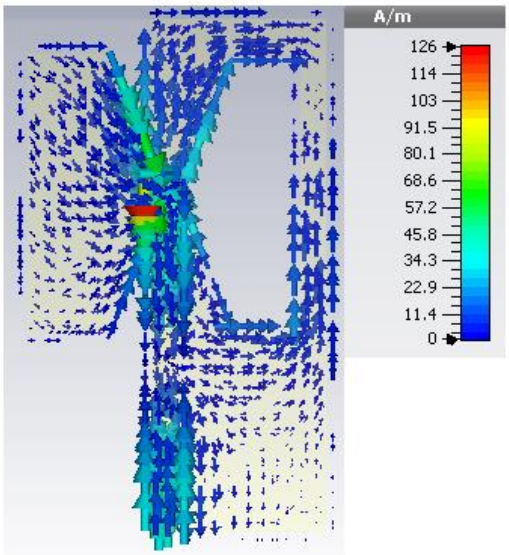

Fig. 4.6: Simulated surface current density of the proposed bow-tie antenna in free space at resonant frequency.

Table 4.2: Performance metrics of the proposed bow-tie antenna in free space

Antenna performance	**Value**
Resonant frequency (GHz)	6.37
S-parameters (dB)	-53.84
Bandwidth (GHz)	5.14
Radiation efficiency (%)	96.87
3-D gain (dB)	3.34
2-D polar gain (dB)	3.23

Fig. 4.5 (a) and Fig. 4.5 (b) depict the simulated far-field 3-D and 2-D polar (recorded at $\theta = 0°$, $\varphi = 90°$) gain patterns of the proposed bow-tie antenna in free space at the resonant frequency of 6.37 GHz. Noticeably, there is a close agreement between the maximum 3-D gain and the 2-D polar main lobe magnitude. Moreover, the half-power beam-width is 252.9°. It is also prominent that the antenna exhibits a quasi-directional radiation pattern, indicating maximum radiation along the bow-tie arms as required for the diagnosis of brain tumor in microwave imaging.

To acquire further insight into the prior discussion on antenna performance, the surface current density is simulated as specified in Fig. 4.6. Apparently, remarkable surface currents are concentrated along the flare regions of the bow-tie arms. Hence, the surface current density is maximum at 126 A/m at 6.37 GHz resonant frequency.

Table 4.2 outlines the performance metrics of the proposed bow-tie antenna in free space with regard to the resonant frequency, S-parameters, bandwidth, radiation efficiency, 3-D gain, and 2-D polar gain that validates its suitability for microwave imaging-based human brain tumor diagnosis as clarified in the next sections.

4.3.4 Antenna with Biological Tissue Model

A six-layered heterogeneous human head phantom model with a spherical shape is proposed as demonstrated in Fig. 4.7 (a). These layers include skin, fat, bone, dura, cerebrospinal fluid (CSF), and brain consecutively [46]. However, the healthy head phantom model is made cancerous by inserting a spherical-shaped malignant tumor of 5 mm radius among dura, CSF, and brain.

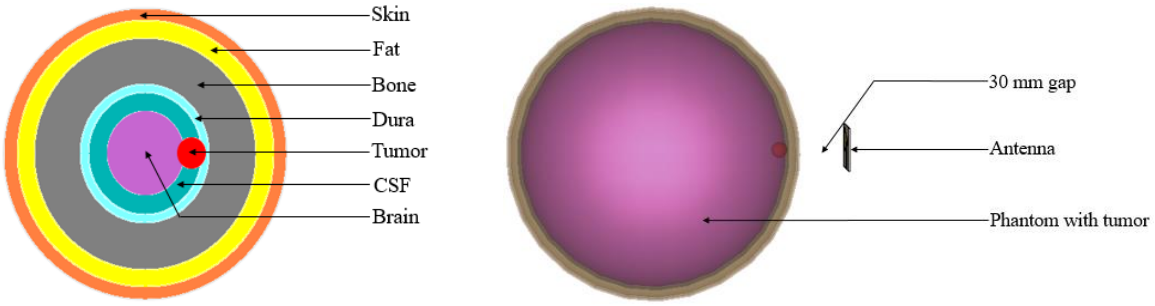

(a) (b)

Fig. 4.7: Six-layered human head phantom model with tumor (a) schematic representation (b) simulation setup.

Table 4.3: Dielectric properties of cancerous human head phantom model with approximate dimensions [47], [48]

Tissue	**Radius (mm)**	**Dielectric properties**		
		Relative permittivity	**Conductivity (S/m)**	**Mass density (kg/m^3)**
Skin	90	45	0.73	1109
Fat	89	5.54	0.04	911
Bone	87.6	5.6	0.03	1908
Dura	83.5	46	0.9	1174
CSF	83	70.1	2.3	1007
Brain	81	43.22	1.29	1046
Tumor	5	55	7	1035.5

It is noteworthy that the model mimics the practical frequency-dependent dielectric properties (i.e., relative permittivity, conductivity, etc.) of a cancerous human head for analyzing the interaction between microwaves and tissue layers properly as mentioned in Table 4.3 [47], [48]. The assessment of antenna performance with the phantom model is accomplished by placing the phantom model at a certain distance of 30 mm from the upper surface of the antenna [49] as shown in Fig. 4.7 (b). This facilitates sufficient penetration of microwave signals inside the tissue layers without causing cumulative side-effects due to antenna radiation. However, the location of the tumor center is at (41.75, 0, 0) mm coordinates from the antenna surface for readily diagnosing it from the simulation results.

4.3.5 Simulation Results with Biological Tissue Model

4.3.5.1 Detection of Brain Tumor

Fig. 4.8 (a) and Fig. 4.8 (b) elucidate the current densities of the proposed bow-tie antenna with phantom in the absence and presence of tumor respectively at the resonant frequency of 6.37 GHz after simulation. It is worth mentioning that the peak value of the antenna current density with phantom and tumor (i.e., 155 A/m^2) is more than two times greater than that with phantom alone (i.e., 60.5 A/m^2). Thus, the proposed antenna can effectively detect the presence of brain tumor with this abrupt rise of current density.

The simulated 10 g average SAR of the proposed bow-tie antenna with phantom in the absence and presence of tumor are highlighted in Fig. 4.9 (a) and Fig. 4.9 (b) chronologically at 6.37 GHz resonant frequency and 0.5 W input reference power.

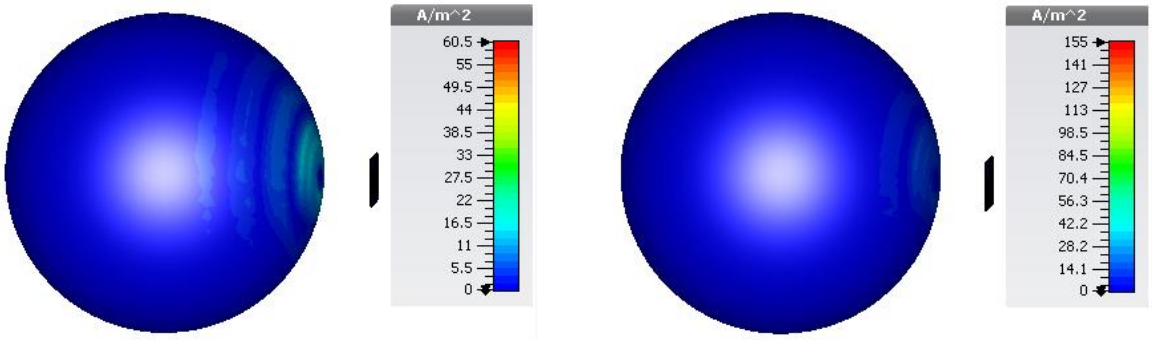

(a) (b)

Fig. 4.8: Simulated current density of the proposed bow-tie antenna at resonant frequency (a) with phantom (b) with phantom and tumor.

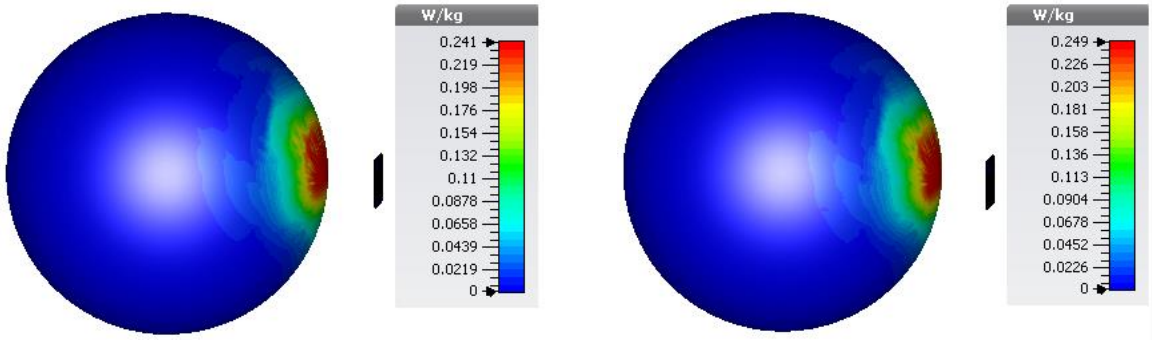

(a) (b)

Fig. 4.9: Simulated SAR distribution of the proposed bow-tie antenna at resonant frequency (a) with phantom (b) with phantom and tumor.

Table 4.4: Performance metrics of the proposed bow-tie antenna with phantom model at resonant frequency

Phantom status	**Peak current density (A/m^2)**	**Peak SAR (W/kg)**
Phantom without tumor	60.5	0.241
Phantom with tumor	155	0.249

Evidently, the peak SAR value of the antenna with phantom containing tumor (i.e., 0.249 W/kg) is higher than that free of tumor (i.e., 0.241 W/kg), implying that the proposed antenna can also detect brain tumor successfully with the excess of SAR distribution result. In addition, it can be observed that the peak value of SAR always lies below 2 W/kg which is the international standard safety limit for 10 g average SAR of bio-tissue [50]. Therefore, no health hazard is supposed to happen in the envisaged detection of brain tumor.

The performance metrics of the proposed bow-tie antenna with the human head phantom model are summarized in Table 4.4 in terms of peak current density and SAR as discussed above. Comparison of these results between healthy and cancerous phantom models confirms the intended brain tumor detection.

4.3.5.2 Localization of Brain Tumor

In order to explicitly visualize the tumor location inside the head phantom, a mechanical rotation of the phantom is performed along its axis by 3.6° angular steps so that it can be horizontally scanned by the antenna in $X-Y$ plane for 100 different positions. During every scanning, a total of 1001 scattering parameters (S_{11}) with tumor and without tumor are measured within the specified UWB frequency range (0 GHz – 12 GHz). For processing these data obtained from CST MWS, the monostatic radar-based delay-and-sum (DAS) beam-forming or confocal microwave imaging algorithm is implemented in MATLAB.

Fig. 4.10 displays the reconstructed microwave image of the brain tumor with a high spatial resolution while Table 4.5 presents the gist of its localization result. It is vivid that the red color signifies the highest intensity value, specifying the tumor location of (49.8, 0.1961) mm coordinates which is close enough to the actual location of (41.75, 0) mm coordinates. Hence, the proposed antenna can identify the brain tumor location inside the human head phantom model with a minimal positive error of (8.05, 0.1961) mm coordinates.

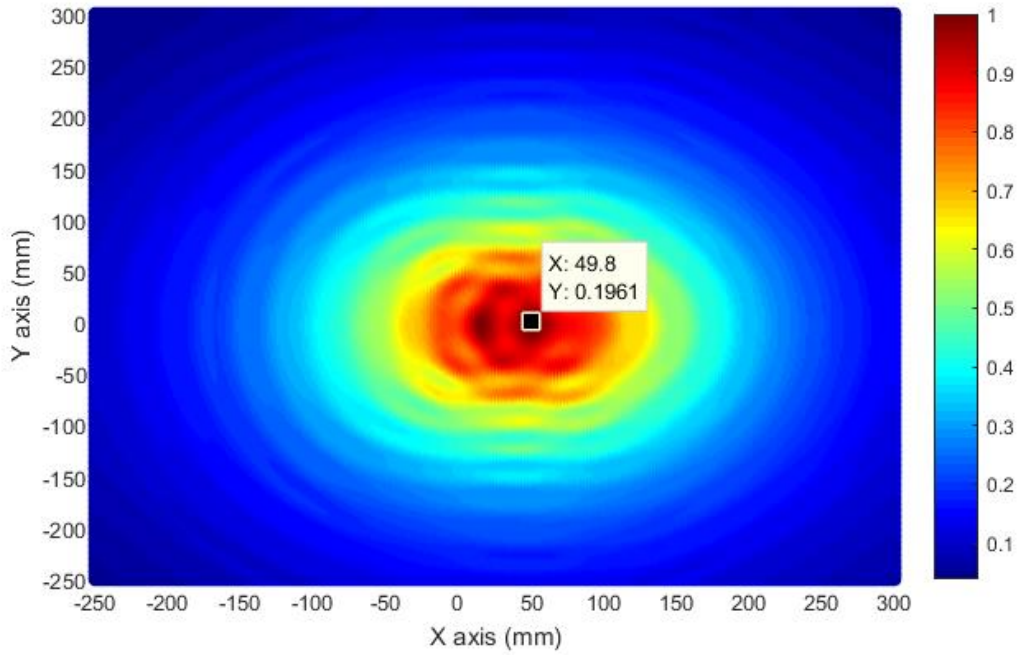

Fig. 4.10: Reconstructed microwave image of brain tumor.

Table 4.5: Localization result of brain tumor

Actual location		**Location in image**		**Localization error**	
X axis (mm)	**Y axis (mm)**	**X axis (mm)**	**Y axis (mm)**	**X axis (mm)**	**Y axis (mm)**
41.75	0	49.8	0.1961	8.05	0.1961

4.4 Proposed Monopole Antenna for Brain Stroke Diagnosis

4.4.1 Antenna Geometry

The geometry of the proposed monopole antenna with specific dimensions of the top view and bottom view is demonstrated in Fig. 4.11 (a) and Fig. 4.11 (b) respectively. The optimum antenna dimensions are given in Table 4.6, followed by the particular design equations. The antenna is derived from a planar rectangular monopole embedded with a trident-shaped or three-branch microstrip feed-line of 50 Ω. Industrially attainable dielectric material Rogers-RO3003 having a relative permittivity (ε_r) of 3, a loss tangent ($tan\delta$) of 0.001, and a thickness (h) of 1.5 mm is chosen as the substrate while annealed copper having a thickness (MT) of 0.035 mm is chosen as the metal. The antenna occupies an overall physical dimension of $30 \times 20 \times 1.5$ mm^3.

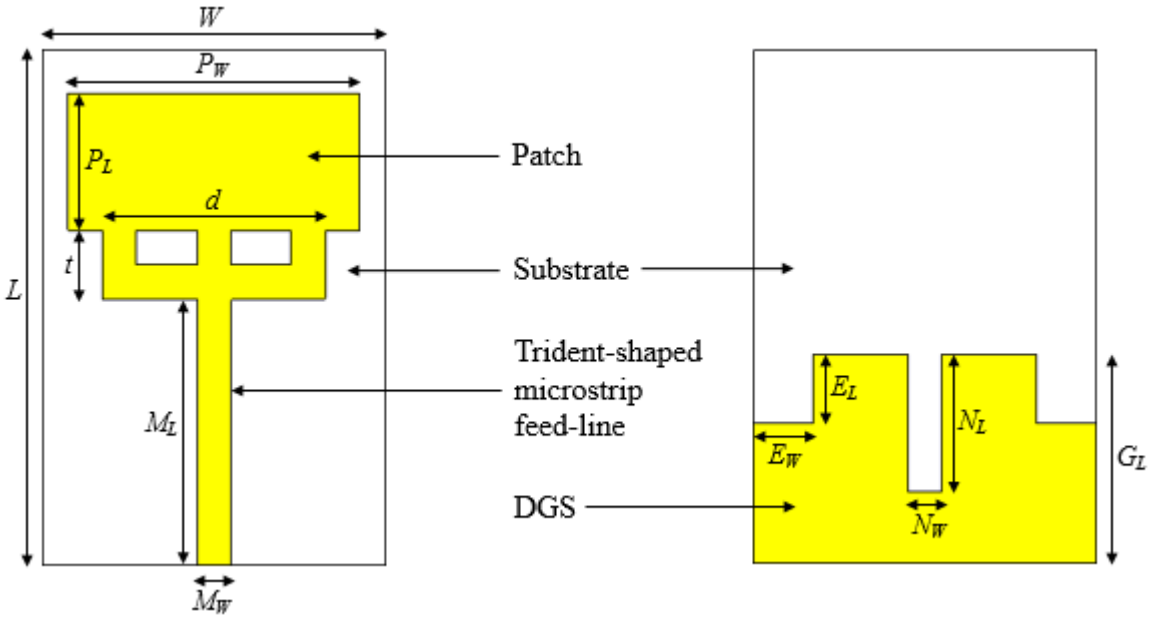

(a) (b)

Fig. 4.11: Geometry of the proposed monopole antenna (a) top view (b) bottom view.

Table 4.6: Optimum dimensions of the proposed monopole antenna

Antenna parameters	**Symbol**	**Value (mm)**
Substrate width	W	20
Substrate length	L	30
Substrate thickness	h	1.5
Metal thickness	MT	0.035
Patch width	P_W	17
Patch length	P_L	8
Microstrip feed width	M_W	2
Microstrip feed length	M_L	15.5
Feed-branch difference	d	13
Feed-branch length	t	4
DGS ground length	G_L	12.2
Edge-cut width	E_W	3.5
Edge-cut length	E_L	4
Notch width	N_W	2
Notch length	N_L	8

The iterative simulation method is utilized to optimize the design parameters so that the antenna input impedance is perfectly matched with the feed-line impedance.

4.4.2 Antenna Design Equations

(i) **Patch width (P_W):** The patch width (P_W) can be deduced as follows [28]:

$$P_W = \frac{\lambda}{3.5} \tag{4.5}$$

Where, λ = center wavelength = c/f; c = velocity of light in vacuum = 3×10^8 m/s; f = center wavelength.

(ii) **Patch length (P_L):** The patch length (P_L) is given by the following equation [28]:

$$P_L = \frac{\lambda}{7.5} \tag{4.6}$$

(iii) **Substrate width (W):** The substrate width (W) is formulated as below [28]:

$$W = P_W + 2h \tag{4.7}$$

Where, h = substrate thickness.

(iv) **Substrate length (L):** The substrate length (L) is determined from the following equation [28]:

$$L = P_L + 15h \tag{4.8}$$

(v) **Feed-branch difference (d):** The feed-branch difference (d) is expressed as follows [28]:

$$d = \frac{P_W}{1.3} \tag{4.9}$$

(vi) **Feed-branch length (t):** The feed-branch length (t) is obtained from the following equation [28]:

$$t = \frac{P_L}{2} \tag{4.10}$$

(vii) **DGS ground length (G_L):** The DGS ground length (G_L) can be calculated as below [28]:

$$G_L = \frac{\lambda}{5} \tag{4.11}$$

(viii) **Edge-cut width (E_W):** The edge-cut width (E_W) is deduced from the following expression:

$$E_W = \frac{W}{2} - \frac{d}{2} \tag{4.12}$$

(ix) **Edge-cut length (E_L):** The edge-cut length (E_L) is identical to the feed-branch length (t) as given below:

$$E_L = t \tag{4.13}$$

(x) **Notch width (N_W):** The notch width (N_W) is equal to the microstrip feed width (M_W) as follows:

$$N_W = M_W \tag{4.14}$$

(xi) **Notch length (N_L):** The notch length (N_L) is derived from the following equation:

$$N_L = \frac{\lambda}{7.5} \tag{4.15}$$

4.4.3 Antenna Design Evolution

The design evolution of the proposed monopole antenna involves four steps as shown chronologically in Fig. 4.12 (a), Fig. 4.12 (b), Fig. 4.12 (c), and Fig. 4.12 (d). In step-1, the basic monopole antenna consists of a radiating metal patch connected to a simple feeding strip on the top layer and a partial metal ground plane on the bottom layer of the substrate, culminating in a planar rectangular structure. Step-2 replaces the simple feeding strip with a two-branch feeding strip of identical widths. In step-3, the two-branch feeding strip is substituted with a trident-shaped feeding strip composed of one central branch and two side branches of equal widths for exciting the antenna symmetrically at three feeding points. The final design step, i.e., step-4 introduces defected ground structure (DGS) by cutting the upper edges of the partial ground plane and inserting a notch in its middle position. The antenna simulation results for each design step are explained thoroughly in the next section.

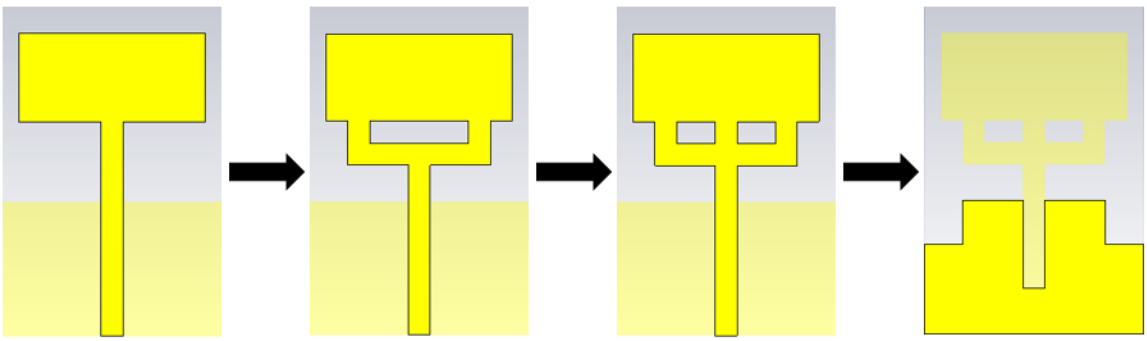

(a) (b) (c) (d)

Fig. 4.12: Design evolution of the proposed monopole antenna (a) step-1 (b) step-2 (c) step-3 (d) step-4.

4.4.4 Simulation Results in Free Space

The step-by-step design and simulation of the proposed monopole antenna are executed in the finite integration technique-based commercial full-wave electromagnetic software package computer simulation technology (CST) microwave studio (MWS). The stepwise simulation results of the antenna in free space are illustrated as follows:

Fig. 4.13 depicts the simulated S_{11} parameters of the proposed monopole antenna in free space for each design step. In step-1, the antenna resonates at 4.5 GHz frequency having 14.43 dB return loss and 1.99 GHz (3.4 GHz - 5.39 GHz) impedance bandwidth. However, in step-2, the antenna resonant frequency is shifted to 3.83 GHz with a higher return loss of 35.71 dB, indicating a better impedance matching and a higher bandwidth of 3.85 GHz (3.08 GHz - 6.93 GHz) than in step-1. The resonant frequency of the antenna is further drifted to 3.79 GHz with an improved return loss and operating bandwidth of 40.19 dB and 4.28 GHz (3.07 GHz - 7.35 GHz) respectively in step-3 compared to step-2. Finally, in step-4, the antenna resonant frequency is tuned to 3.97 GHz with the highest return loss of 50.15 dB and the highest bandwidth of 5.9 GHz ranging from 3.14 GHz to 9.04 GHz among all the steps, making the antenna very promising for microwave imaging-based brain stroke diagnosis.

In Fig. 4.14, the stepwise radiation efficiencies of the proposed monopole antenna after simulation in free space are represented. It can be observed that the antenna achieves a radiation efficiency of 0.754, i.e., 75.4 % at the resonant frequency of 4.5 GHz in step-1.

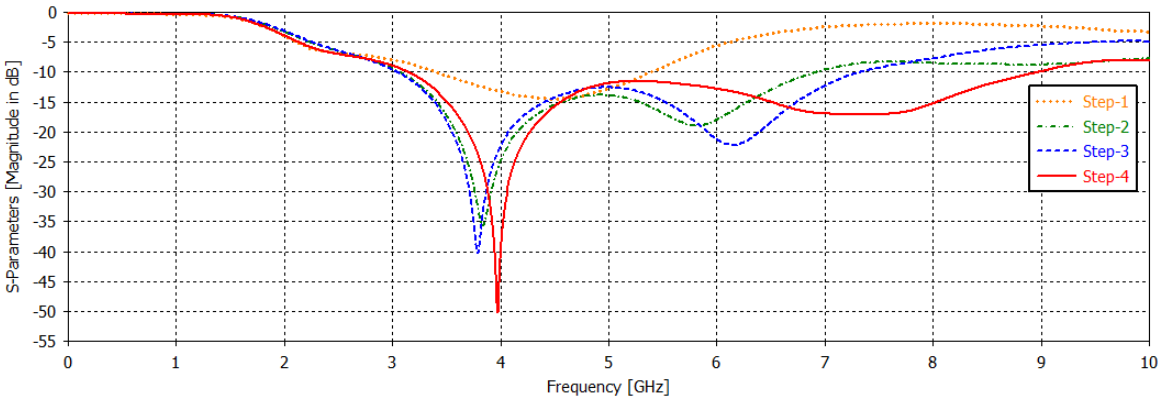

Fig. 4.13: Simulated reflection coefficients (S_{11}) of the proposed monopole antennas in free space for each design step.

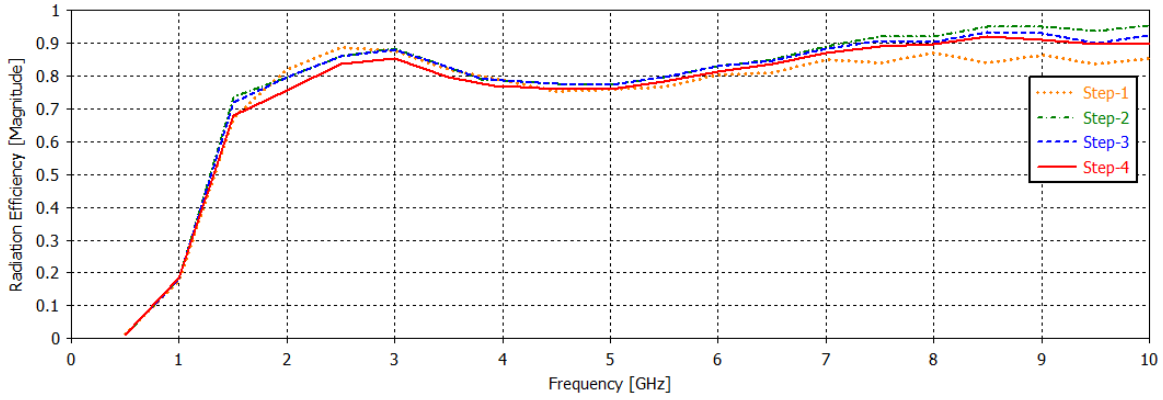

Fig. 4.14: Simulated radiation efficiencies of the proposed monopole antennas in free space for each design step.

Albeit, an augmentation of the radiation efficiency of 0.7876, i.e., 78.76 % at 3.83 GHz resonant frequency occurs in step-2 compared to step-1. Again, in step-3, slightly higher radiation efficiency of 0.7919, i.e., 79.19 % at the resonant frequency of 3.79 GHz is obtained than in step-2. Ultimately, the antenna radiation efficiency is somewhat degraded to 0.765, i.e., 76.5 % at 3.97 GHz resonant frequency in step-4 in contrast to the previous step.

The simulated far-field 3-D gain patterns of the proposed monopole antenna in free space at corresponding resonant frequency for step-1, step-2, step-3, and step-4 are shown in Fig. 4.15(a), Fig. 4.15(b), Fig. 4.15(c), and Fig. 4.15(d) respectively. It is obvious that in step-1, the 3-D gain is maximum at 1.81 dB at 4.5 GHz resonant frequency. However, in step-2, this gain is much enhanced to 2.05 dB at the resonant frequency of 3.83 GHz in comparison to step-1. Furthermore, this gain is merely corroborated to 2.07 dB at 3.79 GHz resonant frequency in step-3 in contrary to the preceding step.

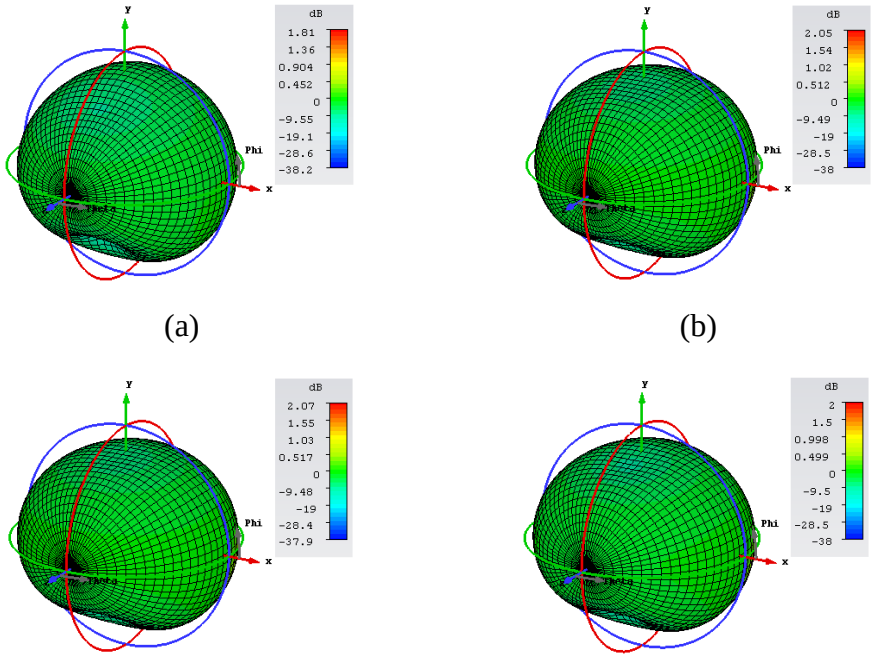

(a) (b)

(c) (d)

Fig. 4.15: Simulated far-field 3-D gain pattern of the proposed monopole antennas in free space at resonant frequency (a) step-1 (b) step-2 (c) step-3 (d) step-4.

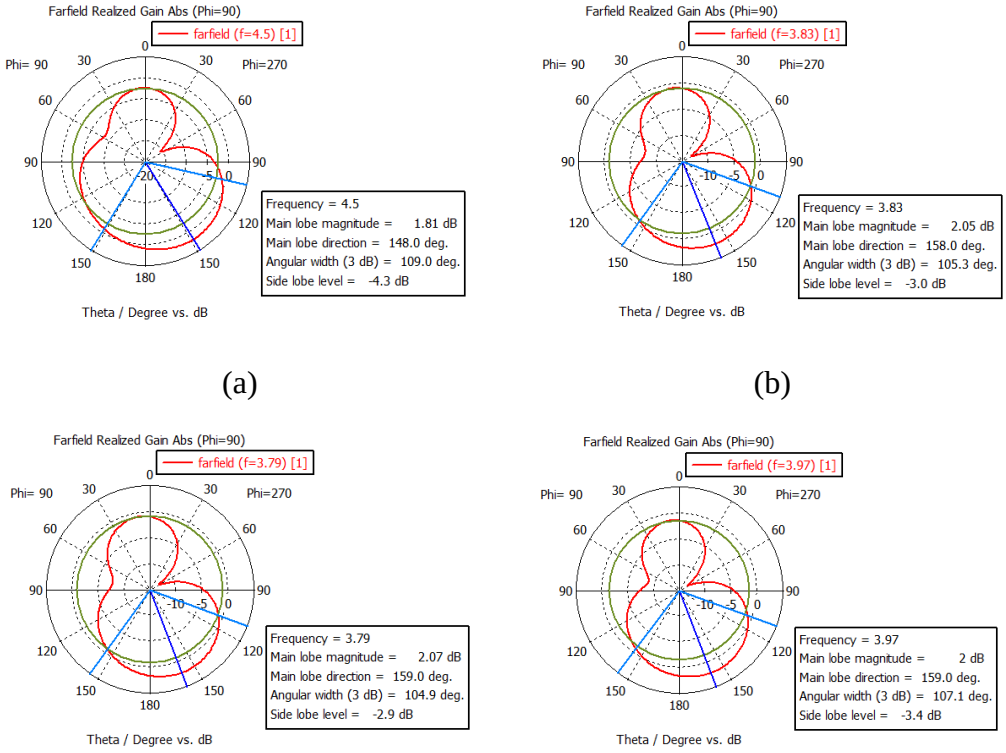

(a) (b)

(c) (d)

Fig. 4.16: Simulated far-field 2-D polar gain pattern of the proposed monopole antennas in free space at resonant frequency (a) step-1 (b) step-2 (c) step-3 (d) step-4.

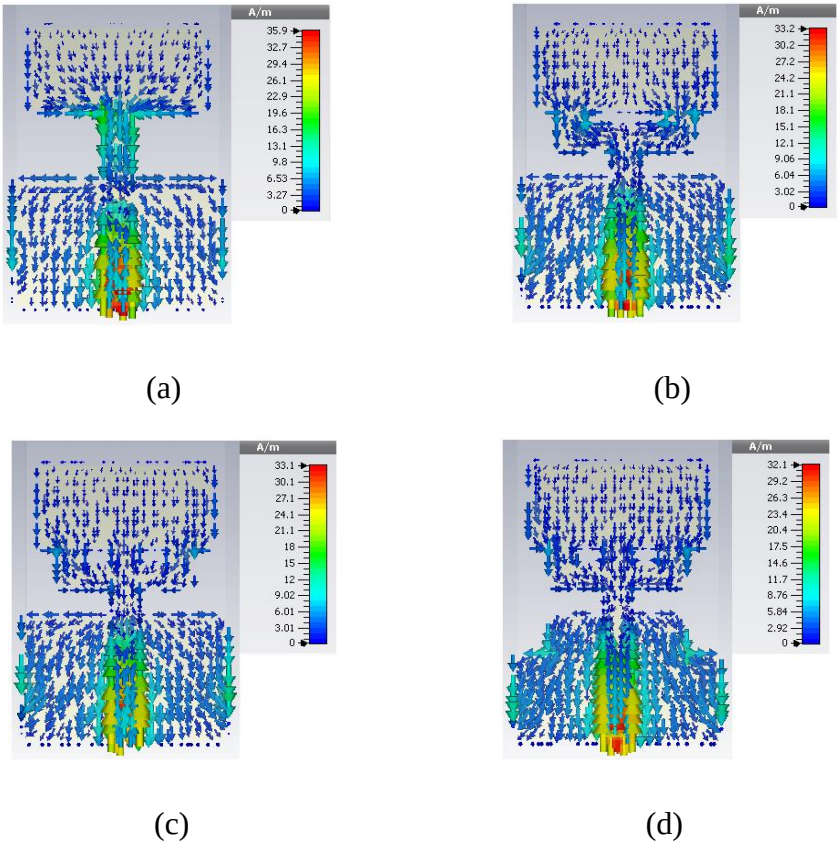

Fig. 4.17: Simulated surface current density of the proposed monopole antennas in free space at resonant frequency (a) step-1 (b) step-2 (c) step-3 (d) step-4.

Table 4.7: Performance metrics of the proposed monopole antenna in free space

Antenna performance	**Step-1**	**Step-2**	**Step-3**	**Step-4**
Resonant frequency (GHz)	4.5	3.83	3.79	3.97
S-parameters (dB)	-14.43	-35.71	-40.19	-50.15
Bandwidth (GHz)	1.99	3.85	4.28	5.9
Radiation efficiency (%)	75.4	78.76	79.19	76.5
3-D gain (dB)	1.81	2.05	2.07	2
2-D polar gain (dB)	1.81	2.05	2.07	2

Eventually, a bit lower 3-D maximum gain of 2 dB prevails in step-4 at the resonant frequency of 3.97 GHz than in step-3.

Fig. 4.16 (a), Fig. 4.16 (b), Fig. 4.16 (c), and Fig. 4.16 (d) demonstrate the simulated far-field 2-D polar gain patterns (observed at $\theta = 0°$, $\varphi = 90°$) of the proposed monopole antenna in free space at individual resonant frequency for step-1, step-2, step-3, and step-4 respectively. Evidently, in step-1, the antenna radiation pattern withholds a semi-directional behavior, pointing maximum radiation to the bottom of the patch having a main lobe

magnitude of 1.81 dB towards 148° direction at 4.5 GHz resonant frequency. In addition, the 3-dB angular beam-width is 109° whereas the side lobe level is -4.3 dB, concentrating maximum power along the major lobe of the antenna. Although, a slight deviation of the radiation pattern occurs in step-2 at the resonant frequency of 3.83 GHz, causing an extended main lobe magnitude of 2.05 dB in the direction of 158° compared to step-1. Also, the 3-dB angular beam-width falls to 105.3° while the side lobe level rises to -3 dB. In step-3, a pretty higher main lobe magnitude of 2.07 dB is found along 159° direction at 3.79 GHz resonant frequency than in step-2. Besides, the 3-dB angular beam-width declines to 104.9° and the side lobe level expands to -2.9 dB. Lastly, in step-4, the main lobe magnitude is lowered to some extent of 2 dB directed towards 159° at the resonant frequency of 3.97 GHz in contrast to the former step. Moreover, the 3-dB angular beam-width is elevated to 107.1° even though the side lobe level is deteriorated to -3.4 dB.

In order to profoundly understand the step-by-step antenna performance as discussed above, the simulated surface current densities are provided in Fig. 4.17 (a), Fig. 4.17 (b), Fig. 4.17 (c), and Fig. 4.17 (d) for step-1, step-2, step-3, and step-4 consecutively at a particular resonant frequency. It is visible that in step-1, significant surface currents are induced along the edges of the partial ground plane at the resonant frequency of 4.5 GHz. In contrast, more uniform surface currents flow through the radiating patch in step-2 at 3.83 GHz resonant frequency. Accordingly, in step-3 at the resonant frequency of 3.79 GHz, much more uniform surface currents are circulated in the entire patch. However, in step-4, strong additional surface currents are adjacent to the edges of the DGS at 3.97 GHz resonant frequency. Consequently, there is a gradual decay in the stepwise maximum surface current density, i.e., 35.9 A/m, 33.2 A/m, 33.1 A/m, and 32.1 A/m obtained for step-1, step-2, step-3, and step-4 respectively.

Table 4.7 highlights the performance metrics of the proposed monopole antenna in free space for each design step. It is nevertheless noteworthy that step-4 is preferable to all other steps, especially in terms of return loss and bandwidth. Therefore, only step-4 is utilized in the following sections to diagnose human brain stroke.

4.4.5 Antenna with Biological Tissue Model

Fig. 4.18 (a) represents a spherical-shaped six-layered heterogeneous human head phantom model that is affected by stroke.

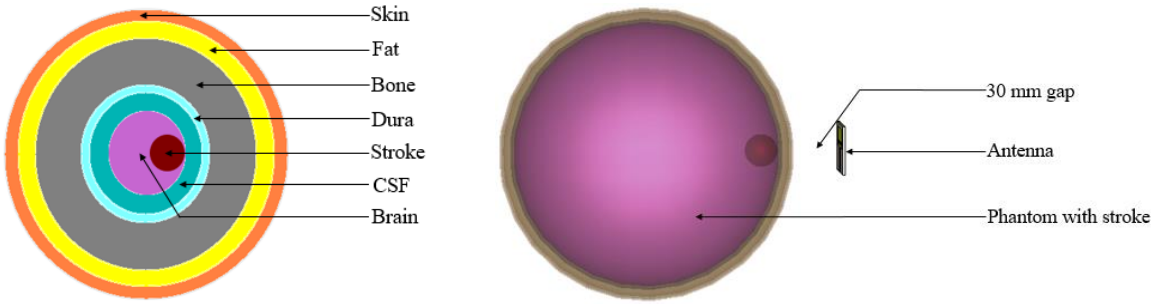

(a) (b)

Fig. 4.18: Six-layered human head phantom model with stroke (a) schematic representation (b) simulation setup.

Table 4.8: Dielectric properties of stroke-affected human head phantom model with approximate dimensions [47], [51]

Tissue		**Radius (mm)**	**Dielectric properties**		
			Relative permittivity	**Conductivity (S/m)**	**Mass density (kg/m^3)**
Skin		90	45	0.73	1109
Fat		89	5.54	0.04	911
Bone		87.6	5.6	0.03	1908
Dura		83.5	46	0.9	1174
CSF		83	70.1	2.3	1007
Brain		81	43.22	1.29	1046
Stroke	Hemorrhagic	10	62	1.5	1050
	Ischemic	10	30	0.5	1060

The six successive layers involve skin, fat, bone, dura, cerebrospinal fluid (CSF), and brain [46] while the stroke might be hemorrhagic or ischemic. Either type of stroke is of 10 mm radius that is individually inserted within the brain intimate to the CSF. It is worth mentioning that the model imitates the realistic frequency-dependent dielectric properties (i.e., relative permittivity, conductivity, and so on) of a stroke-affected human head to appropriately analyze the interactions between microwaves and tissue layers as indicated in Table 4.8 [47], [51]. While assessing antenna performance with the phantom model, a particular distance of 30 mm is retained between the upper surface of the antenna and the phantom model to provide adequate microwave signal penetration within the tissue layers devoid of harmful side-effects caused by antenna radiation [52] as appeared in Fig. 4.18 (b). However, the center of each stroke is located at (49, 0, 0) mm coordinates from the antenna surface so that it can be rapidly diagnosed from the simulation results.

4.4.6 Simulation Results with Biological Tissue Model

4.4.6.1 Detection of Brain Stroke

The current densities of the proposed monopole antenna after simulating with phantom excluding lesion, including a hemorrhagic stroke, and including an ischemic stroke are explicated in Fig. 4.19 (a), Fig. 4.19 (b), and Fig. 4.19 (c) successively at 3.97 GHz resonant frequency. Verily, the peak value of the antenna current density for phantom free of lesion (i.e., 60.5 A/m^2) is less than that containing hemorrhagic stroke (i.e., 61.9 A/m^2) but larger than that containing ischemic stroke (i.e., 59 A/m^2). Thus, the existence of hemorrhagic stroke and ischemic stroke can be detected efficiently with the proposed antenna considering the excess and shortage of current density respectively.

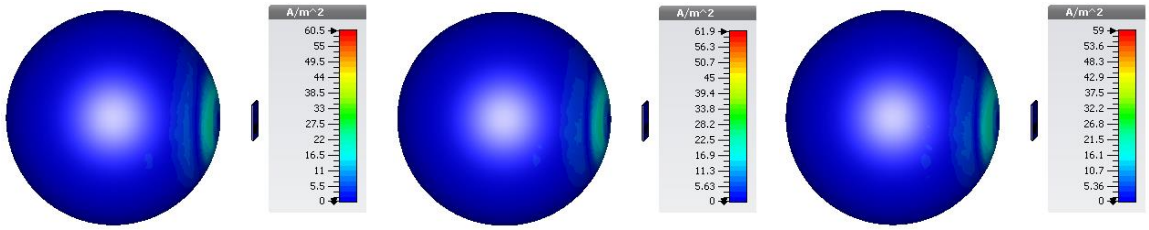

(a) (b) (c)

Fig. 4.19: Simulated current density of the proposed monopole antenna at resonant frequency (a) with phantom (b) with phantom and hemorrhagic stroke (c) with phantom and ischemic stroke.

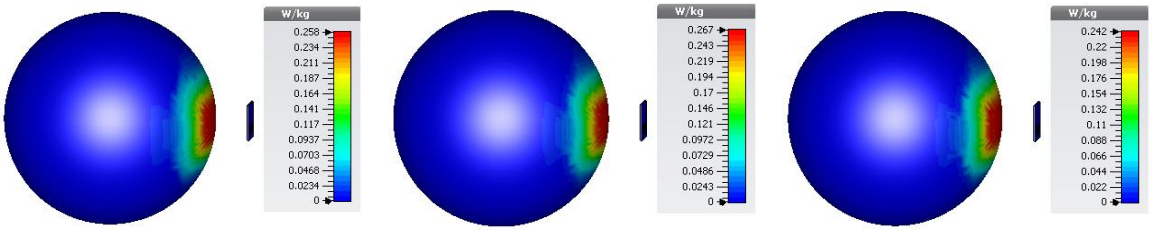

(a) (b) (c)

Fig. 4.20: Simulated SAR distribution of the proposed monopole antenna at resonant frequency (a) with phantom (b) with phantom and hemorrhagic stroke (c) with phantom and ischemic stroke.

Table 4.9: Performance metrics of the proposed monopole antenna with phantom model at resonant frequency

Phantom status	**Peak current density (A/m^2)**	**Peak SAR (W/kg)**
Phantom without lesion	60.5	0.258
Phantom with hemorrhagic stroke	61.9	0.267
Phantom with ischemic stroke	59	0.242

Fig. 4.20 (a), Fig. 4.20 (b), and Fig. 4.20 (c) pictorialize the simulated 10 g average SAR at 0.5 W input reference power and 3.97 GHz resonant frequency of the proposed monopole antenna with phantom having no lesion, having a hemorrhagic stroke, and having an ischemic stroke respectively. It is visible that the peak SAR value of the antenna with phantom alone (i.e., 0.258 W/kg) is smaller than that comprising hemorrhagic stroke (i.e., 0.267 W/kg) albeit higher than that comprising ischemic stroke (i.e., 0.242 W/kg). It indicates that hemorrhagic stroke and ischemic stroke can also be detected with the proposed antenna satisfactorily in order of excessive and deficient SAR distribution. Moreover, it is noteworthy that no health risk is likely to appear in the envisaged brain stroke detection since the peak value of SAR is always lower than the internationally safe and standard SAR limit of bio-tissue for 10 g average, i.e., 2 W/kg [50].

The summary of the performance metrics of the proposed monopole antenna with the human head phantom model is listed in Table 4.9 with regard to peak current density and SAR as interpreted above. Detection of the intended brain stroke is confirmed by simply comparing these results between healthy and stroke-affected phantom models.

4.4.6.2 Localization of Brain Stroke

With a view to visualizing the stroke location explicitly inside the head phantom, the phantom is mechanically rotated by 5.625° angular steps along its axis so that the antenna can sequentially scan the phantom around it in the horizontal $X-Y$ plane for an overall position of 64. At each scan position, altogether 1001 measurement points of scattering parameters (S_{11}) with stroke and without stroke are recorded over the specified UWB frequency band (0 GHz – 10 GHz). The monostatic radar-based delay-and-sum (DAS) beam-forming or confocal microwave imaging algorithm is implemented in MATLAB for processing these data achieved from CST MWS.

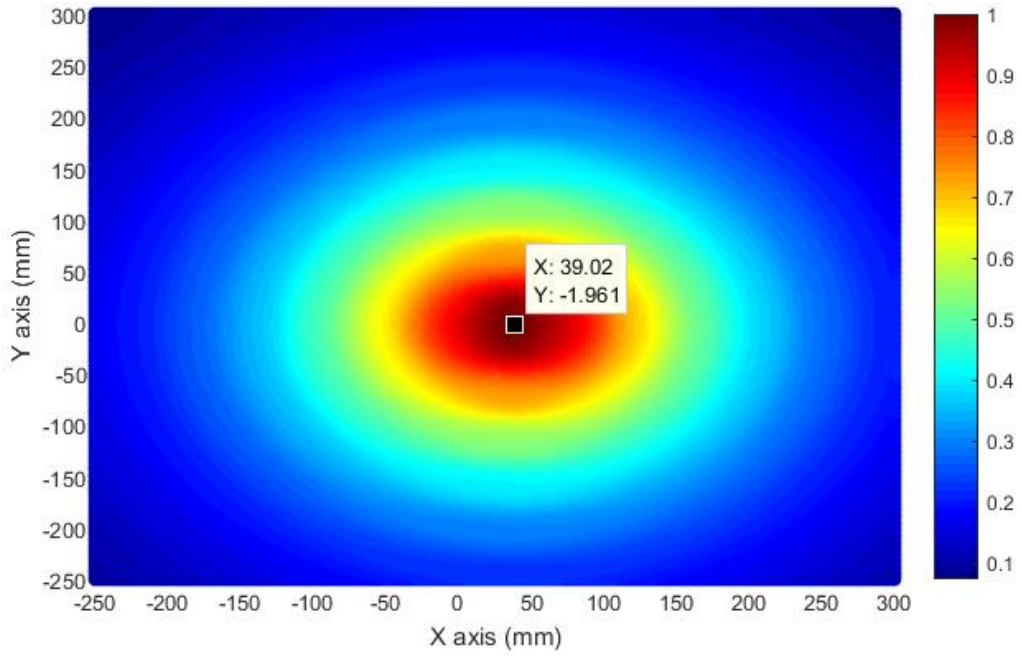

Fig. 4.21: Reconstructed microwave image of brain stroke.

Table 4.10: Localization result of brain stroke

Actual location		**Location in image**		**Localization error**	
X axis (mm)	**Y axis (mm)**	**X axis (mm)**	**Y axis (mm)**	**X axis (mm)**	**Y axis (mm)**
49	0	39.02	-1.961	-9.98	-1.961

The reconstructed microwave image of the brain stroke having a sharp precision is displayed in Fig. 4.21 while the gist of its localization result is presented in Table 4.10. Vividly, the highest intensity value is specified with the red color, implying that the stroke is located at (39.02, -1.961) mm coordinates which is much contiguous to the actual location of (49, 0) mm coordinates. Thus, the location of the brain stroke inside the human head phantom model can be identified with the proposed antenna pertaining to a marginal negative error of (9.98, 1.961) mm coordinates.

4.5 Comparative Analysis

4.5.1 Comparison with Existing Bow-Tie Antennas

The proposed bow-tie antenna is compared with some relevant antennas described in the literature from the perspectives of antenna size, bandwidth, gain, and radiation efficiency as provided in Table 4.11. From this comparison table, it is found that the proposed antenna has the widest bandwidth (i.e., 5.14 GHz) and the highest radiation efficiency (i.e., 96.87 %) in the list. Although, the gain of the proposed antenna (i.e., 3.34 dB) is only higher than that designed by Hossain *et al.* [17] (i.e., -1.42 dB) and Mahalakshmi *et al.* [22] (i.e., -14.5 dB). Apart from the miniaturized antennas developed by Rufus *et al.* [16] (i.e., 16 × 24 × 1.6 mm^3), Arayeshnia *et al.* [18] (i.e., 18 × 18 × 0.5 mm^3), and Mahalakshmi *et al.* [22] (i.e., 10 × 10 × 1 mm^3), the proposed antenna is more compact (i.e., 27 × 17 × 0.787 mm^3) than any other state-of-the-art.

Table 4.11: Comparison among the proposed bow-tie antenna and existing ones

Antenna	**Size (mm^3)**	**Bandwidth (GHz)**	**Gain (dB)**	**Radiation efficiency (%)**
Fiser *et al.*'s work [15]	60 × 60 × 50	5	-	≈80
Rufus *et al.*'s work [16]	16 × 24 × 1.6	0.1	≈5	-
Hossain *et al.*'s work [17]	34.46 × 23.8 × 1.67	0.64	-1.42	75.8
Arayeshnia *et al.*'s work [18]	18 × 18 × 0.5	3.25	-	≈45
Vijayalakshmi *et al.*'s work [19]	57 × 30.4 × 1.6	3.17	4.29	-
Li *et al.*'s work [20]	30 × 30 × 1.27	1.5	≈6	≈91
Gomaa *et al.*'s work [21]	37 × 40 × 1.27	1.8	5	-
Mahalakshmi *et al.*'s work [22]	10 × 10 × 1	≈0.19	-14.5	-
Jalilvand *et al.*'s work [23]	22 × 22 × 1.5	2.4	-	-
Aydin *et al.*'s work [24]	60 × 60 × 2	≈0.2	-	-
Proposed work	27 × 17 × 0.787	5.14	3.34	96.87

4.5.2 Comparison with Existing Monopole Antennas

A comparison among the proposed monopole antenna and some similar antennas reported in the literature are outlined in Table 4.12 from the perspectives of antenna size, bandwidth, gain, and radiation efficiency. It is found from the comparison table that the proposed antenna has the most compact physical dimension (i.e., $30 \times 20 \times 1.5$ mm^3) except for the analogous one designed by Hossain *et al.* [28] and the widest bandwidth (i.e., 5.9 GHz) in the list. Yet, the radiation efficiency of the proposed antenna (i.e., 76.5 %) is inferior to all other state-of-the-art while the gain (i.e., 2 dB) being only higher than that developed by Wu *et al.* [26] (i.e., 1.85 dB).

Table 4.12: Comparison among the proposed monopole antenna and existing ones

Antenna	**Size (mm^3)**	**Bandwidth (GHz)**	**Gain (dB)**	**Radiation efficiency (%)**
Rahman *et al.*'s work [25]	$40 \times 38 \times 1.385$	0.48	2.78	99
Wu *et al.*'s work [26]	$40 \times 40 \times 0.6$	3	1.85	-
Alkasi *et al.*'s work [27]	$81 \times 85 \times 1.6$	0.23	-	-
Hossain *et al.*'s work [28]	$30 \times 20 \times 1.5$	3.85	2.05	78.76
Bhardwaj *et al.*'s work [29]	$40 \times 32 \times 0.8$	3.28	6.8	-
Bashri *et al.*'s work [30]	$70 \times 30 \times 0.075$	2.2	-	-
Talukder *et al.*'s work [31]	$70 \times 60 \times 1.5$	2.37	5.95	93
Vasquez *et al.*'s work [32]	$38 \times 30 \times 1.6$	≈1.22	-	-
Mobashsher *et al.*'s work [33]	$80 \times 45 \times 15$	1.15	3.5	-
Razzicchia *et al.*'s work [34]	$76 \times 38 \times 1.026$	≈0.3	-	-
Proposed work	$30 \times 20 \times 1.5$	5.9	2	76.5

4.6 Discussion

In a nutshell, it can be inferred from the design, simulation, and analysis that the proposed antennas afford a reasonable combination of the most sought-after traits for microwave imaging-based medical applications such as miniature size, enhanced bandwidth, moderate gain, and high radiation efficiency. By means of scrutinizing the specific absorption rate (SAR), a renowned biocompatibility analysis factor, the safety regulation of the human body is preserved in each condition as well. In fact, reliable and simultaneous detection and localization of brain abnormalities are done more precisely and accurately than the existing microwave imaging techniques.

CHAPTER 5
CONCLUSION AND FUTURE RECOMMENDATIONS

5.1 Conclusion

This research work offers an ultra-wideband (UWB) bow-tie antenna and a monopole antenna for the simultaneous detection and localization of brain tumor and brain stroke respectively inside a stratified human head phantom model via microwave imaging scheme. With the proposed self-complementary structure, the performance of the bow-tie antenna is better boosted than the traditional ones. For instance, the antenna occupies a significantly compact size of $27 \times 17 \times 0.787$ mm^3. In addition, it possesses an ultra-wide impedance bandwidth of 5.14 GHz ranging between 5.89 GHz and 11.03 GHz. Moreover, a high radiation efficiency of 96.87 % and a 3-D gain of 3.34 dB are obtained. Likewise, the defected ground structure (DGS) underlying monopole antenna excited by a trident-shaped feeding strip performs superiorly among the prevailing ones. For example, the antenna obtains an ultra-wide impedance bandwidth of 5.9 GHz that ranges from 3.14 GHz to 9.04 GHz. Besides, a radiation efficiency of 76.5 % and a gain of 2 dB are achieved. Furthermore, this miniature antenna occupies an overall volume of $30 \times 20 \times 1.5$ mm^3. Brain tumor detection is confirmed with a significant increase in antenna current density and specific absorption rate (SAR) in contrast to the unwounded tissue. However, the detection of the hemorrhagic stroke is ensured with an excessive antenna current density and SAR while the ischemic stroke is detected with a deficient antenna current density and SAR compared to the normal healthy tissue. In each case, the safety level of SAR is sustained targeting to prevent biohazards. Ultimately, the localization of the brain abnormalities is carried out reliably in two-dimension by developing the monostatic radar-based delay-and-sum (DAS) beam-forming or confocal microwave imaging algorithm to clearly visualize these through image reconstruction. Albeit, the reconstructed microwave images having sharp precision include a minimal positive error and a minimal negative error related to the location of the brain tumor and the brain stroke respectively.

The remainder of this chapter has the following orientation: Section 5.2 addresses the limitations of the work, followed by the future recommendations in Section 5.3.

5.2 Limitations of the Work

Nonetheless, the findings of this research are subjected to several limitations owing to the design and methodological constraints. The notable limitations of this research are addressed as follows:

(i) Being a simulation-based research work, it is conducted thoroughly in software (i.e., CST MWS and MATLAB).

(ii) Because of employing the monostatic approach, simply a single antenna functions as a transceiver from a particular position, and thereby requires an external rotation of the phantom sequentially for a complete scan which is time-consuming.

(iii) Lossy dielectric materials with low relative permittivities (i.e., Rogers-RT5880 with $\varepsilon_r = 2.2$ and Rogers-RO3003 with $\varepsilon_r = 3$) are selected as antenna substrates considering cost-effectiveness.

(iv) Only one type of antenna feeding technique (i.e., microstrip line feed) is utilized due to its design flexibility.

5.3 Future Recommendations

In future, alternative designs and methodologies are imperative to develop for the sake of overcoming the limitations emerged from this research. The following possible approaches are recommended in this aspect:

(i) Practical implementation of the proposed antennas to be tested in the specified application of brain abnormality detection and localization.

(ii) Employment of the multi-static approach where a set of antenna arrays transmits and receives signals from multiple positions for a complete scan, and thereby requires no external rotation of the phantom which is time-saving.

(iii) Selection of antenna substrates from lossy dielectric materials with high relative permittivities (e.g., Rogers-RT6006 with $\varepsilon_r = 6.15$, Taconic CER-10 with $\varepsilon_r = 10$, etc.) to improve the performance metrics.

(iv) Utilization of more antenna feeding techniques (e.g., coaxial probe feed, aperture coupled feed, proximity coupled feed, etc.) for a comparative study.

REFERENCES

[1] Z. Wang, G. Lim, Y. Tang, and M. Leach, "Medical applications of microwave imaging," *The Scientific World Journal,* vol. 2014, pp. 1-7, 2014.

[2] J. Ferlay, I. Soerjomataram, R. Dikshit, S. Eser, C. Mathers, M. Rebelo, D. Parkin, D. Forman, and F. Bray, "Cancer incidence and mortality worldwide: sources, methods and major patterns in GLOBOCAN 2012," *International Journal of Cancer (IJC),* vol. 136, no. 5, pp. 359-386, Mar. 2015.

[3] V. Feigin, M. Samsuzzaman, M. Brainin, B. Norrving, S. Martins, R. Sacco, W. Hacke, M. Fisher, J. Pandian, and P. Lindsay "World stroke organization (WSO): global stroke fact sheet 2022," *International Journal of Stroke,* vol. 17, no. 1, pp. 18-29, Jan. 2022.

[4] Z. Khazaei, E. Goodarzi, V. Borhaninejad, F. Iranmanesh, H. Mirshekarpour, B. Mirzaei, H. Naemi, S. Bechashk, I. Darvishi, R. Sarabi, and A. Tahami, "The association between incidence and mortality of brain cancer and human development index (HDI): an ecological study," *BMC Public Health,* vol. 1696, no. 20, pp. 1-7, 2020.

[5] K. Kabitha, M. Rajan, K. Hegde, S. Koshy, and A. Shenoy, "A comprehensive review on brain tumor," *International Journal of Pharmaceutical, Chemical and Biological Sciences,* vol. 3, no. 4, pp. 1165-1171, 2013.

[6] A. Mobashsher, P. Nguyen, and A. Abbosh, "Detection and localization of brain strokes in realistic 3-D human head phantom," *2013 IEEE MTT-S International Microwave Workshop Series on RF and Wireless Technologies for Biomedical and Healthcare Applications (IMWS-BIO),* pp. 1-3, Dec. 2013.

[7] P. Parmar, "Stroke: classification and diagnosis," *Pharmaceutical Journal,* vol. 10, no. 1, pp. 1-15, Jan. 2018.

[8] S. Hagness, E. Fear, and A. Massa, "Guest editorial: special cluster on microwave medical imaging," *IEEE Antennas and Wireless Propagation Letters,* vol. 11, pp. 1592-1597, 2012.

[9] A. Babu, A. Subhash, D. Rajan, F. Jacob, and P. Kumar, "A survey on methods for brain tumor detection," *IEEE 2018 Conference on Emerging Devices and Smart Systems (ICEDSS),* pp. 213-216, Mar. 2018.

[10] A. Qureshi, Z. Mustansar, and A. Maqsood, "Analysis of microwave scattering from a realistic human head model for brain stroke detection using electromagnetic impedance tomography," *Progress In Electromagnetics Research M,* vol. 52, pp. 45–56, Jan. 2016.

[11] R. Chandra, H. Zhou, I. Balasingham, and R. Narayanan, "On the opportunities and challenges in microwave medical sensing and imaging," *IEEE Transactions on Biomedical Engineering,* vol. 62, no. 7, pp. 1667-1682, 2015.

[12] T. Denidni and G. Augustin, *Ultrawidwband Antennas for Microwave Imaging Systems,* 1st ed., Boston: Artech House, 2014.

[13] D. Ghosh, A. De, M. Taylor, T. Sarkar, M. Wicks, and E. Mokole, "Transmission and reception by ultra-wideband (UWB) antennas," *IEEE Antennas and Propagation. Magazine,* vol. 48, no. 5, pp. 67−99, Oct. 2006.

[14] U. Rafique, S. Pisa, R. Cicchetti, O. Testa, and M. Cavagnaro, "Ultra-wideband antennas for biomedical imaging applications: a survey," *Sensors,* vol. 22, no. 9, pp. 1-38, Apr. 2022.

[15] O. Fiser, V. Hruby, J. Vrba, T. Drizdal, J. Tesarik, J. Junior, and D. Vrba, "UWB bowtie antenna for medical microwave imaging applications," *IEEE Transactions on Antennas and Propagation,* pp. 1-16, Mar. 2022.

[16] E. Rufus, Z. Alex, and P. Chaitanya, "A modified bow-tie antenna for microwave imaging applications," *Journal of Microwaves, Optoelectronics and Electromagnetic Applications,* vol. 7, no. 2, pp. 115-122, Dec. 2008.

[17] A. Hossain and M. Hosain, "Design and simulation of a compact bow-tie antenna for cancer detection and treatment," *2019 4th International Conference on Electrical Information and Communication Technology (EICT),* pp. 1-4, Dec. 2019.

[18] A. Arayeshnia, S. Amiri, and A. Keshtkar, "Miniaturized on-body antenna for small and wearable brain microwave imaging systems," *International Journal of RF and Microwave Computer-Aided Engineering,* vol. 30, no. 1, pp. 1-15, Apr. 2020.

[19] J. Vijayalakshmi and G. Murugesan, "Improved bandwidth and gain in ultra-wideband staircase antipodal bowtie antenna with rounded edge for microwave imaging applications," *Applied Mathematics & Information Sciences,* vol. 12, no. 6, pp. 1197-1202, Nov. 2018.

[20] X. Li, M. Jalilvand, Y. Sit, and T. Zwick, "A compact double-layer on-body matched bowtie antenna for medical diagnosis," *IEEE Transactions on Antennas and Propagation,* vol. 62, no. 4, pp. 1808-1816, Apr. 2014.

[21] A. Gomaa, D. Mohamed, and M. Mangoud, "Double-sided printed triangular bow-tie antenna for UWB communications," *Proceeding of the 17th International Conference on Computer Theory and Applications,* pp. 1-8, Jan. 2007.

[22] N. Mahalakshmi and A. Thenmozhi, "Design of hexagon shape bow-tie patch antenna for implantable bio-medical applications," *Alexandria Engineering Journal,* vol. 56, no. 2, pp. 235-239, June 2017.

[23] M. Jalilvand, X. Li, J. Kowalewski, and T. Zwick, "Broadband miniaturised bow-tie antenna for 3D microwave tomography," *Electronics Letters,* vol. 50, no. 4, pp. 244-246, Feb. 2014.

[24] E. Aydın and A. Torun, "3D printed PLA/copper bowtie antenna for biomedical imaging applications," *Physical and Engineering Sciences in Medicine,* vol. 43, no. 4, pp. 1183-1193, Dec. 2020.

[25] M. Rahman, M. Hossain, M. Riheen, and P. Sekhar, "Early brain stroke detection using flexible monopole antenna," *Progress In Electromagnetics Research C,* vol. 99, pp. 99-110, Jan. 2020.

[26] Y. Wu, M. Wang, and S. Ye, "A compact ultra-wideband antenna for stroke detection," *2016 IEEE International Conference on Microwave and Millimeter Wave Technology (ICMMT),* pp. 546-548, June 2016.

[27] U. Alkasi, T. Caglayan, H. Ahmadzay, and M. Cayoren, "Multiband monopole antenna design for microwave imaging applications," *2015 23nd Signal Processing and Communications Applications Conference (SIU),* pp. 1833-1836, May 2015.

[28] A. Hossain and M. Islam, "Design and optimization of an UWB monopole antenna with a two-branch feeding strip for brain stroke detection," *5th International Conference on Electrical Information and Communication Engineering (EICT),* pp. 1-6, Dec. 2021.

[29] P. Bhardwaj and R. Badhai, "Compact wideband folded strip monopole antenna for brain stroke detection," *International Journal of Microwave and Wireless Technologies,* vol. 13, no. 9, pp. 937-946, Nov. 2021.

[30] M. Bashri, T. Arslan, and W. Zhou, "Flexible antenna array for wearable head imaging system," *2017 11th European Conference on Antennas and Propagation (EUCAP),* pp. 172-176, Mar. 2017.

[31] M. Talukder, M. Samsuzzaman, M. Hasan, M. Islam, G. Bashir, and C. Bepery, "Ellipse shaped patch with ground slotted broadband patch antenna design for microwave head imaging applications," *2020 2nd International Conference on Sustainable Technologies for Industry 4.0 (STI),* pp. 1-5, Dec. 2020.

[32] J. Vasquez, R. Scapaticci, G. Turvani, G. Bellizzi, N. Joachimowicz, B. Duchene, E. Tedeschi, M. Casu, L. Crocco, and F. Vipiana, "Design and experimental assessment of a 2D microwave imaging system for brain stroke monitoring," *International Journal of Antennas and Propagation,* vol. 2019, pp. 1-12, May 2019.

[33] A. Mobashsher and A. Abbosh, "Performance of directional and omnidirectional antennas in wideband head imaging," *IEEE Antennas and Wireless Propagation Letters,* vol. 15, pp. 1618-1621, Jan. 2016.

[34] E. Razzicchia, P. Lu, W. Guo, O. Karadima, I. Sotiriou, N. Ghavami, E. Kallos, G. Palikaras, and P. Kosmas, "Metasurface-enhanced antennas for microwave brain imaging," *Diagnostics,* vol. 11, no. 3, pp. 1-17, Mar. 2021.

[35] A. Faruk and R. Basak, "A novel design and performance analysis of an ISM band antenna for biomedical applications," *AIUB Journal of Science and Engineering (AJSE),* vol. 17, no. 3, pp. 75-82, 2018.

[36] B. Steinberg and H. Subbaram, *Microwave Imaging Techniques,* 1st ed., USA: Wiley-Interscience, pp. 1-361, Apr. 1991.

[37] J. Bolomey and L. Jofre, "Three decades of active microwave imaging achievements, difficulties and future challenges," *2010 IEEE International Conference on Wireless Information Technology and Systems,* pp. 1-4, Oct. 2010.

[38] H. Zhang, A. El-Rayis, N. Haridas, N. Noordin, A. Erdogan, and T. Arslan, "A smart antenna array for brain cancer detection," *2011 Loughborough Antennas & Propagation Conference,* pp. 1-4, Nov. 2011.

[39] R. Inum, M. Rana, K. Shushama, and M. Quader, "EBG based microstrip patch antenna for brain tumor detection via scattering parameters in microwave imaging system," *International Journal of Biomedical Imaging,* vol. 2018, pp. 1-12, Feb. 2018.

[40] D. Miklavcic, N. Pavselj, and F. Hart, "Electric properties of tissues," *Wiley Encyclopedia of Biomedical Engineering,* vol. 101, pp. 1-12, Apr. 2006.

[41] B. Mohammed, A. Abbosh, S. Mustafa, and D. Ireland, "Microwave system for head imaging," *IEEE Transactions on Instrumentation and Measurement,* vol. 63, no. 1, pp. 117-123, Jan. 2014.

[42] S. Semenov, "Microwave tomography: review of the progress towards clinical applications," *Philosophical Transactions of the Royal Society A: Mathematical, Physical and Engineering Sciences,* vol. 367, no. 1900, pp. 3021-3042, Aug. 2009.

[43] A. Balaji, S. Vanaja, C. Malarvizhi, V. Chinnammal, and R. Atla, "Brain tumor detection using radar based design," *High Technology Letters,* vol. 26, no. 6, pp. 168-175, June 2020.

[44] M. Jamlos, W. Mustafa, N. Husna, S. Idrus, W. Khairunizam, I. Zunaidi, Z. Razlan, and S. Bakar, "Ultra-wideband confocal microwave imaging for brain tumor detection," *The 1st International Conference on Mechanical Electronic and Biosystem Engineering (MEBSE),* vol. 557, no. 1, pp. 1-7, Dec 2018.

[45] B. Mohammed, K. Bialkowski, and A. Abbosh, "Radar-based time-domain head imaging using database of effective dielectric constant," *Electronics Letters,* vol. 51, no. 20, pp. 1574-1576, Oct. 2015.

[46] A. Lak and H. Oraizi, "Evaluation of SAR distribution in six-layer human head model," *International Journal of Antennas and Propagation,* vol. 2013, no. 1, pp. 1-8, Jan. 2013.

[47] S. Gabriel, R. Lau, and C. Gabriel, "The dielectric properties of biological tissues: III. parametric models for the dielectric spectrum of tissues," *Physics in Medicine & Biology,* vol. 41, no. 11, pp. 2271-2293, Nov. 1996.

[48] M. Proescholdt, A. Lohmeier, E. Stoerr, P. Eberl, A. Brawanski, Z. Bomzon, and H. Hershkovich, "The dielectric properties of brain tumor tissue," *Neuro-Oncology,* vol. 21, no. 3, pp. 54-55, Sept. 2019.

[49] R. Alagee and A. Assalem, "Brain cancer detection using U-shaped slot vivaldi antenna and confocal radar based microwave imaging algorithm," *American Scientific Research Journal for Engineering, Technology and Sciences (ASRJETS),* vol. 66, no. 1, pp. 1-13, 2020.

[50] IEEE Std. C95.1-2005, "IEEE standards for safety levels with respect to human exposure to radio frequency electromagnetic fields, 3 kHz to 300 GHz," *IEEE International Committee on Electromagnetic Safety (SCC39),* New York, NY, USA: IEEE, pp. 1-238, Apr. 2006.

[51] B. Mohammed, A. Abbosh, and D. Ireland, "Stroke detection based on variations in reflection coefficients of wideband antennas," *Proceedings of the 2012 IEEE International Symposium on Antennas and Propagation,* pp. 1-2, July 2012.

[52] O. Karadima, N. Ghavami, I. Sotiriou, and P. Kosmas, "Performance assessment of microwave tomography and radar imaging using an anthropomorphic brain phantom," *2020 33rd General Assembly and Scientific Symposium of the International Union of Radio Science (URSI GASS),* pp. 1-4, Sept. 2020.

LIST OF PUBLICATIONS

Conference Papers:

(i) A. Hossain and M. Islam, "Design and analysis of a DGS based UWB monopole antenna for brain tumor detection," *2021 5th International Conference on Electrical Engineering and Information & Communication Technology (ICEEICT),* pp. 1-5, Nov. 2021.

(ii) A. Hossain and M. Islam, "Design and optimization of an UWB monopole antenna with a two-branch feeding strip for brain stroke detection," *5th International Conference on Electrical Information and Communication Technology (EICT),* pp. 1-6, Dec. 2021.

Journal Papers:

(i) A. Hossain and M. Islam, "Microwave imaging-based brain tumor detection and localization using UWB self-complementary bow-tie antenna," *(Ready for Submission).*

(ii) A. Hossain and M. Islam, "Microwave imaging-based brain stroke detection and localization using UWB DGS monopole antenna with a trident-shaped feeding strip," *(Ready for Submission).*

APPENDIX

MATLAB Code for Microwave Image Reconstruction of Brain Tumor:

```
clc
clear all
%%S11 data acquisition with tumor from CST (Phantom with tumor rotation
by 3.6°)
load S_1.txt;load S_2.txt;load S_3.txt;load S_4.txt;
load S_5.txt;load S_6.txt;load S_7.txt;load S_8.txt;
load S_9.txt;load S_10.txt;load S_11.txt;load S_12.txt;
load S_13.txt;load S_14.txt;load S_15.txt;load S_16.txt;
load S_17.txt;load S_18.txt;load S_19.txt;load S_20.txt;
load S_21.txt;load S_22.txt;load S_23.txt;load S_24.txt;
load S_25.txt;load S_26.txt;load S_27.txt;load S_28.txt;
load S_29.txt;load S_30.txt;load S_31.txt;load S_32.txt;
load S_33.txt;load S_34.txt;load S_35.txt;load S_36.txt;
load S_37.txt;load S_38.txt;load S_39.txt;load S_40.txt;
load S_41.txt;load S_42.txt;load S_43.txt;load S_44.txt;
load S_45.txt;load S_46.txt;load S_47.txt;load S_48.txt;
load S_49.txt;load S_50.txt;load S_51.txt;load S_52.txt;
load S_53.txt;load S_54.txt;load S_55.txt;load S_56.txt;
load S_57.txt;load S_58.txt;load S_59.txt;load S_60.txt;
load S_61.txt;load S_62.txt;load S_63.txt;load S_64.txt;
load S_65.txt;load S_66.txt;load S_67.txt;load S_68.txt;
load S_69.txt;load S_70.txt;load S_71.txt;load S_72.txt;
load S_73.txt;load S_74.txt;load S_75.txt;load S_76.txt;
load S_77.txt;load S_78.txt;load S_79.txt;load S_80.txt;
load S_81.txt;load S_82.txt;load S_83.txt;load S_84.txt;
load S_85.txt;load S_86.txt;load S_87.txt;load S_88.txt;
load S_89.txt;load S_90.txt;load S_91.txt;load S_92.txt;
load S_93.txt;load S_94.txt;load S_95.txt;load S_96.txt;
load S_97.txt;load S_98.txt;load S_99.txt;load S_100.txt;
a_1=db2mag(S_1(:,2)');a_2=db2mag(S_2(:,2)');a_3=db2mag(S_3(:,2)');
a_4=db2mag(S_4(:,2)');a_5=db2mag(S_5(:,2)');a_6=db2mag(S_6(:,2)');
a_7=db2mag(S_7(:,2)');a_8=db2mag(S_8(:,2)');a_9=db2mag(S_9(:,2)');
a_10=db2mag(S_10(:,2)');a_11=db2mag(S_11(:,2)');a_12=db2mag(S_12(:,2)');
a_13=db2mag(S_13(:,2)');a_14=db2mag(S_14(:,2)');a_15=db2mag(S_15(:,2)');
a_16=db2mag(S_16(:,2)');a_17=db2mag(S_17(:,2)');a_18=db2mag(S_18(:,2)');
a_19=db2mag(S_19(:,2)');a_20=db2mag(S_20(:,2)');a_21=db2mag(S_21(:,2)');
a_22=db2mag(S_22(:,2)');a_23=db2mag(S_23(:,2)');a_24=db2mag(S_24(:,2)');
a_25=db2mag(S_25(:,2)');a_26=db2mag(S_26(:,2)');a_27=db2mag(S_27(:,2)');
a_28=db2mag(S_28(:,2)');a_29=db2mag(S_29(:,2)');a_30=db2mag(S_30(:,2)');
a_31=db2mag(S_31(:,2)');a_32=db2mag(S_32(:,2)');a_33=db2mag(S_33(:,2)');
a_34=db2mag(S_34(:,2)');a_35=db2mag(S_35(:,2)');a_36=db2mag(S_36(:,2)');
a_37=db2mag(S_37(:,2)');a_38=db2mag(S_38(:,2)');a_39=db2mag(S_39(:,2)');
a_40=db2mag(S_40(:,2)');a_41=db2mag(S_41(:,2)');a_42=db2mag(S_42(:,2)');
a_43=db2mag(S_43(:,2)');a_44=db2mag(S_44(:,2)');a_45=db2mag(S_45(:,2)');
a_46=db2mag(S_46(:,2)');a_47=db2mag(S_47(:,2)');a_48=db2mag(S_48(:,2)');
a_49=db2mag(S_49(:,2)');a_50=db2mag(S_50(:,2)');a_51=db2mag(S_51(:,2)');
a_52=db2mag(S_52(:,2)');a_53=db2mag(S_53(:,2)');a_54=db2mag(S_54(:,2)');
a_55=db2mag(S_55(:,2)');a_56=db2mag(S_56(:,2)');a_57=db2mag(S_57(:,2)');
a_58=db2mag(S_58(:,2)');a_59=db2mag(S_59(:,2)');a_60=db2mag(S_60(:,2)');
a_61=db2mag(S_61(:,2)');a_62=db2mag(S_62(:,2)');a_63=db2mag(S_63(:,2)');
a_64=db2mag(S_64(:,2)');a_65=db2mag(S_65(:,2)');a_66=db2mag(S_66(:,2)');
a_67=db2mag(S_67(:,2)');a_68=db2mag(S_68(:,2)');a_69=db2mag(S_69(:,2)');
a_70=db2mag(S_70(:,2)');a_71=db2mag(S_71(:,2)');a_72=db2mag(S_72(:,2)');
a_73=db2mag(S_73(:,2)');a_74=db2mag(S_74(:,2)');a_75=db2mag(S_75(:,2)');
a_76=db2mag(S_76(:,2)');a_77=db2mag(S_77(:,2)');a_78=db2mag(S_78(:,2)');
a_79=db2mag(S_79(:,2)');a_80=db2mag(S_80(:,2)');a_81=db2mag(S_81(:,2)');
```

```
a_82=db2mag(S_82(:,2)');a_83=db2mag(S_83(:,2)');a_84=db2mag(S_84(:,2)');
a_85=db2mag(S_85(:,2)');a_86=db2mag(S_86(:,2)');a_87=db2mag(S_87(:,2)');
a_88=db2mag(S_88(:,2)');a_89=db2mag(S_89(:,2)');a_90=db2mag(S_90(:,2)');
a_91=db2mag(S_91(:,2)');a_92=db2mag(S_92(:,2)');a_93=db2mag(S_93(:,2)');
a_94=db2mag(S_94(:,2)');a_95=db2mag(S_95(:,2)');a_96=db2mag(S_96(:,2)');
a_97=db2mag(S_97(:,2)');a_98=db2mag(S_98(:,2)');a_99=db2mag(S_99(:,2)');
a_100=db2mag(S_100(:,2)');
with_tumor=[a_1
    a_2
    a_3
    a_4
    a_5
    a_6
    a_7
    a_8
    a_9
    a_10
    a_11
    a_12
    a_13
    a_14
    a_15
    a_16
    a_17
    a_18
    a_19
    a_20
    a_21
    a_22
    a_23
    a_24
    a_25
    a_26
    a_27
    a_28
    a_29
    a_30
    a_31
    a_32
    a_33
    a_34
    a_35
    a_36
    a_37
    a_38
    a_39
    a_40
    a_41
    a_42
    a_43
    a_44
    a_45
    a_46
    a_47
    a_48
    a_49
    a_50
    a_51
    a_52
    a_53
    a_54
```

```
    a_55
    a_56
    a_57
    a_58
    a_59
    a_60
    a_61
    a_62
    a_63
    a_64
    a_65
    a_66
    a_67
    a_68
    a_69
    a_70
    a_71
    a_72
    a_73
    a_74
    a_75
    a_76
    a_77
    a_78
    a_79
    a_80
    a_81
    a_82
    a_83
    a_84
    a_85
    a_86
    a_87
    a_88
    a_89
    a_90
    a_91
    a_92
    a_93
    a_94
    a_95
    a_96
    a_97
    a_98
    a_99
    a_100]';
%%S11 data acquisition without tumor from CST (Phantom rotation by 3.6°)
load R_1.txt;load R_2.txt;load R_3.txt;load R_4.txt;
load R_5.txt;load R_6.txt;load R_7.txt;load R_8.txt;
load R_9.txt;load R_10.txt;load R_11.txt;load R_12.txt;
load R_13.txt;load R_14.txt;load R_15.txt;load R_16.txt;
load R_17.txt;load R_18.txt;load R_19.txt;load R_20.txt;
load R_21.txt;load R_22.txt;load R_23.txt;load R_24.txt;
load R_25.txt;load R_26.txt;load R_27.txt;load R_28.txt;
load R_29.txt;load R_30.txt;load R_31.txt;load R_32.txt;
load R_33.txt;load R_34.txt;load R_35.txt;load R_36.txt;
load R_37.txt;load R_38.txt;load R_39.txt;load R_40.txt;
load R_41.txt;load R_42.txt;load R_43.txt;load R_44.txt;
load R_45.txt;load R_46.txt;load R_47.txt;load R_48.txt;
load R_49.txt;load R_50.txt;load R_51.txt;load R_52.txt;
load R_53.txt;load R_54.txt;load R_55.txt;load R_56.txt;
```

```
load R_57.txt;load R_58.txt;load R_59.txt;load R_60.txt;
load R_61.txt;load R_62.txt;load R_63.txt;load R_64.txt;
load R_65.txt;load R_66.txt;load R_67.txt;load R_68.txt;
load R_69.txt;load R_70.txt;load R_71.txt;load R_72.txt;
load R_73.txt;load R_74.txt;load R_75.txt;load R_76.txt;
load R_77.txt;load R_78.txt;load R_79.txt;load R_80.txt;
load R_81.txt;load R_82.txt;load R_83.txt;load R_84.txt;
load R_85.txt;load R_86.txt;load R_87.txt;load R_88.txt;
load R_89.txt;load R_90.txt;load R_91.txt;load R_92.txt;
load R_93.txt;load R_94.txt;load R_95.txt;load R_96.txt;
load R_97.txt;load R_98.txt;load R_99.txt;load R_100.txt;
b_1=db2mag(R_1(:,2)');b_2=db2mag(R_2(:,2)');b_3=db2mag(R_3(:,2)');
b_4=db2mag(R_4(:,2)');b_5=db2mag(R_5(:,2)');b_6=db2mag(R_6(:,2)');
b_7=db2mag(R_7(:,2)');b_8=db2mag(R_8(:,2)');b_9=db2mag(R_9(:,2)');
b_10=db2mag(R_10(:,2)');b_11=db2mag(R_11(:,2)');b_12=db2mag(R_12(:,2)');
b_13=db2mag(R_13(:,2)');b_14=db2mag(R_14(:,2)');b_15=db2mag(R_15(:,2)');
b_16=db2mag(R_16(:,2)');b_17=db2mag(R_17(:,2)');b_18=db2mag(R_18(:,2)');
b_19=db2mag(R_19(:,2)');b_20=db2mag(R_20(:,2)');b_21=db2mag(R_21(:,2)');
b_22=db2mag(R_22(:,2)');b_23=db2mag(R_23(:,2)');b_24=db2mag(R_24(:,2)');
b_25=db2mag(R_25(:,2)');b_26=db2mag(R_26(:,2)');b_27=db2mag(R_27(:,2)');
b_28=db2mag(R_28(:,2)');b_29=db2mag(R_29(:,2)');b_30=db2mag(R_30(:,2)');
b_31=db2mag(R_31(:,2)');b_32=db2mag(R_32(:,2)');b_33=db2mag(R_33(:,2)');
b_34=db2mag(R_34(:,2)');b_35=db2mag(R_35(:,2)');b_36=db2mag(R_36(:,2)');
b_37=db2mag(R_37(:,2)');b_38=db2mag(R_38(:,2)');b_39=db2mag(R_39(:,2)');
b_40=db2mag(R_40(:,2)');b_41=db2mag(R_41(:,2)');b_42=db2mag(R_42(:,2)');
b_43=db2mag(R_43(:,2)');b_44=db2mag(R_44(:,2)');b_45=db2mag(R_45(:,2)');
b_46=db2mag(R_46(:,2)');b_47=db2mag(R_47(:,2)');b_48=db2mag(R_48(:,2)');
b_49=db2mag(R_49(:,2)');b_50=db2mag(R_50(:,2)');b_51=db2mag(R_51(:,2)');
b_52=db2mag(R_52(:,2)');b_53=db2mag(R_53(:,2)');b_54=db2mag(R_54(:,2)');
b_55=db2mag(R_55(:,2)');b_56=db2mag(R_56(:,2)');b_57=db2mag(R_57(:,2)');
b_58=db2mag(R_58(:,2)');b_59=db2mag(R_59(:,2)');b_60=db2mag(R_60(:,2)');
b_61=db2mag(R_61(:,2)');b_62=db2mag(R_62(:,2)');b_63=db2mag(R_63(:,2)');
b_64=db2mag(R_64(:,2)');b_65=db2mag(R_65(:,2)');b_66=db2mag(R_66(:,2)');
b_67=db2mag(R_67(:,2)');b_68=db2mag(R_68(:,2)');b_69=db2mag(R_69(:,2)');
b_70=db2mag(R_70(:,2)');b_71=db2mag(R_71(:,2)');b_72=db2mag(R_72(:,2)');
b_73=db2mag(R_73(:,2)');b_74=db2mag(R_74(:,2)');b_75=db2mag(R_75(:,2)');
b_76=db2mag(R_76(:,2)');b_77=db2mag(R_77(:,2)');b_78=db2mag(R_78(:,2)');
b_79=db2mag(R_79(:,2)');b_80=db2mag(R_80(:,2)');b_81=db2mag(R_81(:,2)');
b_82=db2mag(R_82(:,2)');b_83=db2mag(R_83(:,2)');b_84=db2mag(R_84(:,2)');
b_85=db2mag(R_85(:,2)');b_86=db2mag(R_86(:,2)');b_87=db2mag(R_87(:,2)');
b_88=db2mag(R_88(:,2)');b_89=db2mag(R_89(:,2)');b_90=db2mag(R_90(:,2)');
b_91=db2mag(R_91(:,2)');b_92=db2mag(R_92(:,2)');b_93=db2mag(R_93(:,2)');
b_94=db2mag(R_94(:,2)');b_95=db2mag(R_95(:,2)');b_96=db2mag(R_96(:,2)');
b_97=db2mag(R_97(:,2)');b_98=db2mag(R_98(:,2)');b_99=db2mag(R_99(:,2)');
b_100=db2mag(R_100(:,2)');
without_tumor=[b_1
    b_2
    b_3
    b_4
    b_5
    b_6
    b_7
    b_8
    b_9
    b_10
    b_11
    b_12
    b_13
    b_14
    b_15
    b_16
```

b_17
b_18
b_19
b_20
b_21
b_22
b_23
b_24
b_25
b_26
b_27
b_28
b_29
b_30
b_31
b_32
b_33
b_34
b_35
b_36
b_37
b_38
b_39
b_40
b_41
b_42
b_43
b_44
b_45
b_46
b_47
b_48
b_49
b_50
b_51
b_52
b_53
b_54
b_55
b_56
b_57
b_58
b_59
b_60
b_61
b_62
b_63
b_64
b_65
b_66
b_67
b_68
b_69
b_70
b_71
b_72
b_73
b_74
b_75
b_76
b_77

```
    b_78
    b_79
    b_80
    b_81
    b_82
    b_83
    b_84
    b_85
    b_86
    b_87
    b_88
    b_89
    b_90
    b_91
    b_92
    b_93
    b_94
    b_95
    b_96
    b_97
    b_98
    b_99
    b_100]';
%%Windowing using Hamming window
[A,B]=size(with_tumor);%A=Number of rows=1001,B=Number of columns=100
[A,B]=size(without_tumor);
Window=hamming(A);
with_window=zeros(A,B);
without_window=zeros(A,B);
for k=1:B
    with_window(:,k)=with_tumor(:,k).*Window;
    without_window(:,k)=without_tumor(:,k).*Window;
end
%%Frequency domain to time domain conversion
Time_resolution=(A-1)/(max(R_1(:,1)*1e9)-
min(R_1(:,1)*1e9));%R(:,1)=S(:,1)=Frequency[GHz]
Sample_size=Time_resolution/(A-1);
Time=linspace(-(A-1)/2*Sample_size,(A-1)/2*Sample_size,A);
IFFT_with=ifftshift(ifft(with_window));
IFFT_without=ifftshift(ifft(without_window));
%%Calibration
Calibrated_with=IFFT_with-IFFT_without;
%%Clutter removal
Average=zeros(A,10);
i=1;
for k=1:B
    Average(:,i)=Average(:,i)+Calibrated_with(:,k);
    if rem(k,10)==0
        i=i+1;
    end
end
Average=Average./10;
New_with=zeros(A,B);
i=1;
for k=1:B
    New_with(:,k)=Calibrated_with(:,k)-Average(:,i);
    if rem(k,10)==0
        i=i+1;
    end
end
Processed_signal=abs(New_with);
```

```
%%Synthetic focusing(Air)
[a,b]=meshgrid(linspace(0,0,10),linspace(0,90,10));
X=b(:)';%Scan position(horizontal coordinate)[mm]
Y=a(:)';%Scan position(vertical coordinate)[mm]
[x,y]=meshgrid(linspace(-250,300,256),linspace(-250,300,256));
x=x(:);%Focal point(horizontal coordinate)[mm]
y=y(:);%Focal point(vertical coordinate)[mm]
D_air=30;%Distance between antenna and phantom[mm]
d_air=zeros(length(x),B);%Propagation distance for air[mm]
for k=1:B
    for m=1:length(x)
        D=sqrt((X(k)-x(m))^2+(Y(k)-y(m))^2);
        d_air(m,k)=sqrt(D^2+D_air^2);
    end
end
Epsilonr_air=1;%Relative permitivity of air
c=3e11;%Light velocity[mm]
vdelta_air=c/sqrt(Epsilonr_air);%Propagation velocity for air
t_air=zeros(length(x),B);%Round-trip time for air
for k=1:B
    for i=1:length(x)
        t_air(i,k)=2*d_air(i,k)/vdelta_air;
    end
end
%%Synthetic focusing(Skin)
d_skin=1;%Skin thickness[mm]
Epsilonr_skin=45;%Relative permitivity of skin
vdelta_skin=c/sqrt(Epsilonr_skin);%Propagation velocity for skin
t_skin=zeros(length(x),B);%Round-trip time for skin
for k=1:B
    for i=1:length(x)
        t_skin(i,k)=2*d_skin/vdelta_skin;
    end
end
%%Synthetic focusing(Fat)
d_fat=1.4;%Fat thickness[mm]
Epsilonr_fat=5.54;%Relative permitivity of fat
vdelta_fat=c/sqrt(Epsilonr_fat);%Propagation velocity for fat
t_fat=zeros(length(x),B);%Round-trip time for fat
for k=1:B
    for i=1:length(x)
        t_fat(i,k)=2*d_fat/vdelta_fat;
    end
end
%%Synthetic focusing(Bone)
d_bone=4.1;%Bone thickness[mm]
Epsilonr_bone=5.6;%Relative permitivity of bone
vdelta_bone=c/sqrt(Epsilonr_bone);%Propagation velocity for bone
t_bone=zeros(length(x),B);%Round-trip time for bone
for k=1:B
    for i=1:length(x)
        t_bone(i,k)=2*d_bone/vdelta_bone;
    end
end
%%Synthetic focusing(Dura)
d_dura=0.5;%Dura thickness[mm]
Epsilonr_dura=46;%Relative permitivity of dura
vdelta_dura=c/sqrt(Epsilonr_dura);%Propagation velocity for dura
t_dura=zeros(length(x),B);%Round-trip time for dura
for k=1:B
    for i=1:length(x)
```

```
        t_dura(i,k)=2*d_dura/vdelta_dura;
    end
end
%%Synthetic focusing(CSF)
d_CSF=2;%CSF thickness[mm]
Epsilonr_CSF=70.1;%Relative permitivity of CSF
vdelta_CSF=c/sqrt(Epsilonr_CSF);%Propagation velocity for CSF
t_CSF=zeros(length(x),B);%Round-trip time for CSF
for k=1:B
    for i=1:length(x)
        t_CSF(i,k)=2*d_CSF/vdelta_CSF;
    end
end
%%Synthetic focusing(Brain)
d_brain=81;%Brain thickness[mm]
Epsilonr_brain=43.22;%Relative permitivity of brain
vdelta_brain=c/sqrt(Epsilonr_brain);%Propagation velocity for brain
t_brain=zeros(length(x),B);%Round-trip time for brain
for k=1:B
    for i=1:length(x)
        t_brain(i,k)=2*d_brain/vdelta_brain;
    end
end
%%Synthetic focusing(Total)
t_total=zeros(length(x),B);%Total round-trip time
for k=1:B
    for i=1:length(x)
    t_total(i,k)=t_air(i,k)+t_skin(i,k)+ t_fat(i,k)+t_bone(i,k)+
    t_dura(i,k)+t_CSF(i,k)+t_brain(i,k);
    end
end
%%Image generation
Interpolated_data=zeros(length(t_total),B);%Spline interpolation
for k=1:B
    Interpolated_data(:,k)=interp1(Time, Processed_signal(:,k),
    t_total(:,k),'spline');
end
Intensity_values=zeros(length(Interpolated_data),1);%Intensity values
associated with the pixel points
for j=1:length(Interpolated_data)
    Intensity_values(j)=sum(Interpolated_data(j,:));
end
Intensity_values=Intensity_values./max(Intensity_values);
Intensity=Intensity_values.^4;
figure('Name','Figure : Reconstructed Image','NumberTitle','Off');%Image
mapping
scatter(x,y,500,Intensity,'.');
axis([min(x) max(x) min(y) max(y)]);
xlabel('X axis (mm)')
ylabel('Y axis (mm)')
colorbar
```

MATLAB Code for Microwave Image Reconstruction of Brain Stroke:

```
clc
clear all
%%S11 data acquisition with stroke from CST (Phantom with stroke
rotation by 5.625°)
load S_1.txt;load S_2.txt;load S_3.txt;load S_4.txt;
load S_5.txt;load S_6.txt;load S_7.txt;load S_8.txt;
```

```
load S_9.txt;load S_10.txt;load S_11.txt;load S_12.txt;
load S_13.txt;load S_14.txt;load S_15.txt;load S_16.txt;
load S_17.txt;load S_18.txt;load S_19.txt;load S_20.txt;
load S_21.txt;load S_22.txt;load S_23.txt;load S_24.txt;
load S_25.txt;load S_26.txt;load S_27.txt;load S_28.txt;
load S_29.txt;load S_30.txt;load S_31.txt;load S_32.txt;
load S_33.txt;load S_34.txt;load S_35.txt;load S_36.txt;
load S_37.txt;load S_38.txt;load S_39.txt;load S_40.txt;
load S_41.txt;load S_42.txt;load S_43.txt;load S_44.txt;
load S_45.txt;load S_46.txt;load S_47.txt;load S_48.txt;
load S_49.txt;load S_50.txt;load S_51.txt;load S_52.txt;
load S_53.txt;load S_54.txt;load S_55.txt;load S_56.txt;
load S_57.txt;load S_58.txt;load S_59.txt;load S_60.txt;
load S_61.txt;load S_62.txt;load S_63.txt;load S_64.txt;
a_1=db2mag(S_1(:,2)');a_2=db2mag(S_2(:,2)');a_3=db2mag(S_3(:,2)');
a_4=db2mag(S_4(:,2)');a_5=db2mag(S_5(:,2)');a_6=db2mag(S_6(:,2)');
a_7=db2mag(S_7(:,2)');a_8=db2mag(S_8(:,2)');a_9=db2mag(S_9(:,2)');
a_10=db2mag(S_10(:,2)');a_11=db2mag(S_11(:,2)');a_12=db2mag(S_12(:,2)');
a_13=db2mag(S_13(:,2)');a_14=db2mag(S_14(:,2)');a_15=db2mag(S_15(:,2)');
a_16=db2mag(S_16(:,2)');a_17=db2mag(S_17(:,2)');a_18=db2mag(S_18(:,2)');
a_19=db2mag(S_19(:,2)');a_20=db2mag(S_20(:,2)');a_21=db2mag(S_21(:,2)');
a_22=db2mag(S_22(:,2)');a_23=db2mag(S_23(:,2)');a_24=db2mag(S_24(:,2)');
a_25=db2mag(S_25(:,2)');a_26=db2mag(S_26(:,2)');a_27=db2mag(S_27(:,2)');
a_28=db2mag(S_28(:,2)');a_29=db2mag(S_29(:,2)');a_30=db2mag(S_30(:,2)');
a_31=db2mag(S_31(:,2)');a_32=db2mag(S_32(:,2)');a_33=db2mag(S_33(:,2)');
a_34=db2mag(S_34(:,2)');a_35=db2mag(S_35(:,2)');a_36=db2mag(S_36(:,2)');
a_37=db2mag(S_37(:,2)');a_38=db2mag(S_38(:,2)');a_39=db2mag(S_39(:,2)');
a_40=db2mag(S_40(:,2)');a_41=db2mag(S_41(:,2)');a_42=db2mag(S_42(:,2)');
a_43=db2mag(S_43(:,2)');a_44=db2mag(S_44(:,2)');a_45=db2mag(S_45(:,2)');
a_46=db2mag(S_46(:,2)');a_47=db2mag(S_47(:,2)');a_48=db2mag(S_48(:,2)');
a_49=db2mag(S_49(:,2)');a_50=db2mag(S_50(:,2)');a_51=db2mag(S_51(:,2)');
a_52=db2mag(S_52(:,2)');a_53=db2mag(S_53(:,2)');a_54=db2mag(S_54(:,2)');
a_55=db2mag(S_55(:,2)');a_56=db2mag(S_56(:,2)');a_57=db2mag(S_57(:,2)');
a_58=db2mag(S_58(:,2)');a_59=db2mag(S_59(:,2)');a_60=db2mag(S_60(:,2)');
a_61=db2mag(S_61(:,2)');a_62=db2mag(S_62(:,2)');a_63=db2mag(S_63(:,2)');
a_64=db2mag(S_64(:,2)');
with_stroke=[a_1
    a_2
    a_3
    a_4
    a_5
    a_6
    a_7
    a_8
    a_9
    a_10
    a_11
    a_12
    a_13
    a_14
    a_15
    a_16
    a_17
    a_18
    a_19
    a_20
    a_21
    a_22
    a_23
    a_24
    a_25
```

```
    a_26
    a_27
    a_28
    a_29
    a_30
    a_31
    a_32
    a_33
    a_34
    a_35
    a_36
    a_37
    a_38
    a_39
    a_40
    a_41
    a_42
    a_43
    a_44
    a_45
    a_46
    a_47
    a_48
    a_49
    a_50
    a_51
    a_52
    a_53
    a_54
    a_55
    a_56
    a_57
    a_58
    a_59
    a_60
    a_61
    a_62
    a_63
    a_64]';
%%S11 data acquisition without stroke from CST (Phantom rotation by
5.625°)
load R_1.txt;load R_2.txt;load R_3.txt;load R_4.txt;
load R_5.txt;load R_6.txt;load R_7.txt;load R_8.txt;
load R_9.txt;load R_10.txt;load R_11.txt;load R_12.txt;
load R_13.txt;load R_14.txt;load R_15.txt;load R_16.txt;
load R_17.txt;load R_18.txt;load R_19.txt;load R_20.txt;
load R_21.txt;load R_22.txt;load R_23.txt;load R_24.txt;
load R_25.txt;load R_26.txt;load R_27.txt;load R_28.txt;
load R_29.txt;load R_30.txt;load R_31.txt;load R_32.txt;
load R_33.txt;load R_34.txt;load R_35.txt;load R_36.txt;
load R_37.txt;load R_38.txt;load R_39.txt;load R_40.txt;
load R_41.txt;load R_42.txt;load R_43.txt;load R_44.txt;
load R_45.txt;load R_46.txt;load R_47.txt;load R_48.txt;
load R_49.txt;load R_50.txt;load R_51.txt;load R_52.txt;
load R_53.txt;load R_54.txt;load R_55.txt;load R_56.txt;
load R_57.txt;load R_58.txt;load R_59.txt;load R_60.txt;
load R_61.txt;load R_62.txt;load R_63.txt;load R_64.txt;
b_1=db2mag(R_1(:,2)');b_2=db2mag(R_2(:,2)');b_3=db2mag(R_3(:,2)');
b_4=db2mag(R_4(:,2)');b_5=db2mag(R_5(:,2)');b_6=db2mag(R_6(:,2)');
b_7=db2mag(R_7(:,2)');b_8=db2mag(R_8(:,2)');b_9=db2mag(R_9(:,2)');
```

```
b_10=db2mag(R_10(:,2)');b_11=db2mag(R_11(:,2)');b_12=db2mag(R_12(:,2)');
b_13=db2mag(R_13(:,2)');b_14=db2mag(R_14(:,2)');b_15=db2mag(R_15(:,2)');
b_16=db2mag(R_16(:,2)');b_17=db2mag(R_17(:,2)');b_18=db2mag(R_18(:,2)');
b_19=db2mag(R_19(:,2)');b_20=db2mag(R_20(:,2)');b_21=db2mag(R_21(:,2)');
b_22=db2mag(R_22(:,2)');b_23=db2mag(R_23(:,2)');b_24=db2mag(R_24(:,2)');
b_25=db2mag(R_25(:,2)');b_26=db2mag(R_26(:,2)');b_27=db2mag(R_27(:,2)');
b_28=db2mag(R_28(:,2)');b_29=db2mag(R_29(:,2)');b_30=db2mag(R_30(:,2)');
b_31=db2mag(R_31(:,2)');b_32=db2mag(R_32(:,2)');b_33=db2mag(R_33(:,2)');
b_34=db2mag(R_34(:,2)');b_35=db2mag(R_35(:,2)');b_36=db2mag(R_36(:,2)');
b_37=db2mag(R_37(:,2)');b_38=db2mag(R_38(:,2)');b_39=db2mag(R_39(:,2)');
b_40=db2mag(R_40(:,2)');b_41=db2mag(R_41(:,2)');b_42=db2mag(R_42(:,2)');
b_43=db2mag(R_43(:,2)');b_44=db2mag(R_44(:,2)');b_45=db2mag(R_45(:,2)');
b_46=db2mag(R_46(:,2)');b_47=db2mag(R_47(:,2)');b_48=db2mag(R_48(:,2)');
b_49=db2mag(R_49(:,2)');b_50=db2mag(R_50(:,2)');b_51=db2mag(R_51(:,2)');
b_52=db2mag(R_52(:,2)');b_53=db2mag(R_53(:,2)');b_54=db2mag(R_54(:,2)');
b_55=db2mag(R_55(:,2)');b_56=db2mag(R_56(:,2)');b_57=db2mag(R_57(:,2)');
b_58=db2mag(R_58(:,2)');b_59=db2mag(R_59(:,2)');b_60=db2mag(R_60(:,2)');
b_61=db2mag(R_61(:,2)');b_62=db2mag(R_62(:,2)');b_63=db2mag(R_63(:,2)');
b_64=db2mag(R_64(:,2)');
without_stroke=[b_1
    b_2
    b_3
    b_4
    b_5
    b_6
    b_7
    b_8
    b_9
    b_10
    b_11
    b_12
    b_13
    b_14
    b_15
    b_16
    b_17
    b_18
    b_19
    b_20
    b_21
    b_22
    b_23
    b_24
    b_25
    b_26
    b_27
    b_28
    b_29
    b_30
    b_31
    b_32
    b_33
    b_34
    b_35
    b_36
    b_37
    b_38
    b_39
    b_40
    b_41
    b_42
```

```
    b_43
    b_44
    b_45
    b_46
    b_47
    b_48
    b_49
    b_50
    b_51
    b_52
    b_53
    b_54
    b_55
    b_56
    b_57
    b_58
    b_59
    b_60
    b_61
    b_62
    b_63
    b_64]';
%%Windowing using Hamming window
[A,B]=size(with_stroke);%A=Number of rows=1001,B=Number of columns=64
[A,B]=size(without_stroke);
Window=hamming(A);
with_window=zeros(A,B);
without_window=zeros(A,B);
for k=1:B
    with_window(:,k)=with_stroke(:,k).*Window;
    without_window(:,k)=without_stroke(:,k).*Window;
end
%%Frequency domain to time domain conversion
Time_resolution=(A-1)/(max(R_1(:,1)*1e9)-
min(R_1(:,1)*1e9));%R(:,1)=S(:,1)=Frequency[GHz]
Sample_size=Time_resolution/(A-1);
Time=linspace(-(A-1)/2*Sample_size,(A-1)/2*Sample_size,A);
IFFT_with=ifftshift(ifft(with_window));
IFFT_without=ifftshift(ifft(without_window));
%%Calibration
Calibrated_with=IFFT_with-IFFT_without;
%%Clutter removal
Average=zeros(A,8);
i=1;
for k=1:B
    Average(:,i)=Average(:,i)+Calibrated_with(:,k);
    if rem(k,8)==0
        i=i+1;
    end
end
Average=Average./8;
New_with=zeros(A,B);
i=1;
for k=1:B
    New_with(:,k)=Calibrated_with(:,k)-Average(:,i);
    if rem(k,8)==0
        i=i+1;
    end
end
Processed_signal=abs(New_with);
%%Synthetic focusing(Air)
```

```
[a,b]=meshgrid(linspace(0,0,8),linspace(0,90,8));
X=b(:)';%Scan position(horizontal coordinate)[mm]
Y=a(:)';%Scan position(vertical coordinate)[mm]
[x,y]=meshgrid(linspace(-250,300,256),linspace(-250,300,256));
x=x(:);%Focal point(horizontal coordinate)[mm]
y=y(:);%Focal point(vertical coordinate)[mm]
D_air=30;%Distance between antenna and phantom[mm]
d_air=zeros(length(x),B);%Propagation distance for air[mm]
for k=1:B
    for m=1:length(x)
        D=sqrt((X(k)-x(m))^2+(Y(k)-y(m))^2);
        d_air(m,k)=sqrt(D^2+D_air^2);
    end
end
Epsilonr_air=1;%Relative permitivity of air
c=3e11;%Light velocity[mm]
vdelta_air=c/sqrt(Epsilonr_air);%Propagation velocity for air
t_air=zeros(length(x),B);%Round-trip time for air
for k=1:B
    for i=1:length(x)
        t_air(i,k)=2*d_air(i,k)/vdelta_air;
    end
end
%%Synthetic focusing(Skin)
d_skin=1;%Skin thickness[mm]
Epsilonr_skin=45;%Relative permitivity of skin
vdelta_skin=c/sqrt(Epsilonr_skin);%Propagation velocity for skin
t_skin=zeros(length(x),B);%Round-trip time for skin
for k=1:B
    for i=1:length(x)
        t_skin(i,k)=2*d_skin/vdelta_skin;
    end
end
%%Synthetic focusing(Fat)
d_fat=1.4;%Fat thickness[mm]
Epsilonr_fat=5.54;%Relative permitivity of fat
vdelta_fat=c/sqrt(Epsilonr_fat);%Propagation velocity for fat
t_fat=zeros(length(x),B);%Round-trip time for fat
for k=1:B
    for i=1:length(x)
        t_fat(i,k)=2*d_fat/vdelta_fat;
    end
end
%%Synthetic focusing(Bone)
d_bone=4.1;%Bone thickness[mm]
Epsilonr_bone=5.6;%Relative permitivity of bone
vdelta_bone=c/sqrt(Epsilonr_bone);%Propagation velocity for bone
t_bone=zeros(length(x),B);%Round-trip time for bone
for k=1:B
    for i=1:length(x)
        t_bone(i,k)=2*d_bone/vdelta_bone;
    end
end
%%Synthetic focusing(Dura)
d_dura=0.5;%Dura thickness[mm]
Epsilonr_dura=46;%Relative permitivity of dura
vdelta_dura=c/sqrt(Epsilonr_dura);%Propagation velocity for dura
t_dura=zeros(length(x),B);%Round-trip time for dura
for k=1:B
    for i=1:length(x)
        t_dura(i,k)=2*d_dura/vdelta_dura;
```

```
    end
end
%%Synthetic focusing(CSF)
d_CSF=2;%CSF thickness[mm]
Epsilonr_CSF=70.1;%Relative permitivity of CSF
vdelta_CSF=c/sqrt(Epsilonr_CSF);%Propagation velocity for CSF
t_CSF=zeros(length(x),B);%Round-trip time for CSF
for k=1:B
    for i=1:length(x)
        t_CSF(i,k)=2*d_CSF/vdelta_CSF;
    end
end
%%Synthetic focusing(Brain)
d_brain=81;%Brain thickness[mm]
Epsilonr_brain=43.22;%Relative permitivity of brain
vdelta_brain=c/sqrt(Epsilonr_brain);%Propagation velocity for brain
t_brain=zeros(length(x),B);%Round-trip time for brain
for k=1:B
    for i=1:length(x)
        t_brain(i,k)=2*d_brain/vdelta_brain;
    end
end
%%Synthetic focusing(Total)
t_total=zeros(length(x),B);%Total round-trip time
for k=1:B
    for i=1:length(x)
    t_total(i,k)=t_air(i,k)+t_skin(i,k)+t_fat(i,k)+t_bone(i,k)+
    t_dura(i,k)+t_CSF(i,k)+t_brain(i,k);
    end
end
%%Image generation
Interpolated_data=zeros(length(t_total),B);%Spline interpolation
for k=1:B
    Interpolated_data(:,k)=interp1(Time,Processed_signal(:,k),
    t_total(:,k),'spline');
end
Intensity_values=zeros(length(Interpolated_data),1);%Intensity values
associated with the pixel points
for j=1:length(Interpolated_data)
    Intensity_values(j)=sum(Interpolated_data(j,:));
end
Intensity_values=Intensity_values./max(Intensity_values);
Intensity=Intensity_values.^4;
figure('Name','Figure : Reconstructed Image','NumberTitle','Off');%Image
mapping
scatter(x,y,500,Intensity,'.');
axis([min(x) max(x) min(y) max(y)]);
xlabel('X axis (mm)')
ylabel('Y axis (mm)')
colorbar
```